

---

# A NUMERICAL INVESTIGATION OF TBA.....!!!1

---

BY H.G.K.G JAYATUNGA

A THESIS SUBMITTED TO MONASH UNIVERSITY IN FULFILMENT OF THE REQUIREMENTS  
FOR THE DEGREE OF

DOCTOR OF PHILOSOPHY

Department of Mechanical Engineering

Monash University

Date .....!!!!!!







*“Dedicated to Mrs. Malin Bamunuarachchi whom without this work would not see the light of day. Thank you madam for your prayers, blessings, guidance, kind words of encourgaement and above all, believeing in me and giving me strength to get back up when I myslef have given up hope....”*



# CONTENTS

---

<b>1</b>	<b>A review of the literature</b>	<b>1</b>
1.1	Flow induced vibrations . . . . .	1
1.2	Fluid-elastic galloping . . . . .	1
1.2.1	Excitation of galloping . . . . .	1
1.2.2	Quasi-steady state theory . . . . .	2
1.2.3	Induced force and the shear layers . . . . .	5
1.2.4	Frequency response . . . . .	7
1.2.5	Fluid mechanics governing the galloping response . . . . .	7
1.2.6	Galloping as a mechanism of energy harvesting . . . . .	8
<b>2</b>	<b>Methodology and validation</b>	<b>11</b>
2.1	Introduction . . . . .	11
2.1.1	Parameters used . . . . .	11
2.2	Quasi-steady model . . . . .	12
	Solving the quasi-steady state equation . . . . .	13
2.3	Calculation of average power . . . . .	13
2.4	Direct numerical simulations (DNS) . . . . .	14
2.4.1	Governing equations . . . . .	14
2.4.2	Temporal discretisation:Time-splitting . . . . .	16
	Integration of the substep equations . . . . .	17
	The convection substep . . . . .	17
	The pressure substep . . . . .	20
	The diffusion substep . . . . .	20
	Special discretisation:Spectral element method . . . . .	21

## CONTENTS

---

Boundary conditions . . . . .	25
2.4.3 Convergence and validation studies . . . . .	25
Domain size . . . . .	25
Convergence . . . . .	26
<b>3 Governing parameters of fluid-elastic galloping</b>	<b>28</b>
3.1 Introduction . . . . .	28
3.1.1 Static body results . . . . .	29
3.2 Formulation of the non-dimensionalised parameters $\Pi_1$ and $\Pi_2$ . . . . .	30
3.3 Quasi-steady state results . . . . .	33
3.3.1 Classical VIV parameters vs. $\Pi_1$ and $\Pi_2$ . . . . .	33
3.3.2 High and low $Re$ data . . . . .	35
3.3.3 Dependence on mass-stiffness, $\Pi_1$ . . . . .	37
3.3.4 Dependence on the mass ratio $m^*$ . . . . .	40
3.3.5 Comparison with DNS data . . . . .	40
3.4 Summary of the governing parameters of fluid-elastic galloping . . . . .	48
<b>4 Frequency response of the system</b>	<b>50</b>
4.1 Introduction . . . . .	50
4.2 Linear frequency of the system . . . . .	50
4.3 Finding the terminal velocity of the body when no frequency is predicted by equation 8 . . . . .	51
<b>5 Influence of fluid dynamics of the system on the extracted power</b>	<b>53</b>
5.1 Introduction . . . . .	53
5.2 Influence of the shear layers . . . . .	54
5.3 Static body results . . . . .	55
5.4 QSS results . . . . .	57
5.4.1 Mean power output . . . . .	57
5.4.2 Surface pressure . . . . .	58
5.4.3 Velocity profiles at the leading edges . . . . .	58
5.5 Fluid-structure interaction (DNS) results . . . . .	62







# CHAPTER 1

---

## A REVIEW OF THE LITERATURE

### 1.1 Flow induced vibrations

### 1.2 Fluid-elastic galloping

Fluid-elastic galloping is one of the most commonly observable flow-induced vibration on a slender body. Since this phenomenon is most common in civil structure, such as buildings and iced-transmission lines, the term “aeroelastic galloping” is commonly used as the body is immersed in air. However, this mechanism can occur on a slender body immersed in any Newtonian fluid, provided that the conditions to sustain the galloping mechanism are satisfied. This work is based on a general Newtonian flow, thus the term “ fluid-elastic galloping” is used throughout this thesis.

#### 1.2.1 Excitation of galloping

Païdoussis et al. (2010) describes galloping as a “velocity dependent and damping controlled” phenomenon. Therefore, in order for a body to gallop, an initial excitation has to be given to that body. While this excitation is mainly caused by the force created from vortex shedding, other fluid instabilities may contribute to this initial excitation. When a bluff body moves along the transverse direction of the fluid flow, it generates a force along the transverse direction. This force, also known as the induced lift is a resultant of the velocity of the fluid and the motion of the body. When this body is attached to an

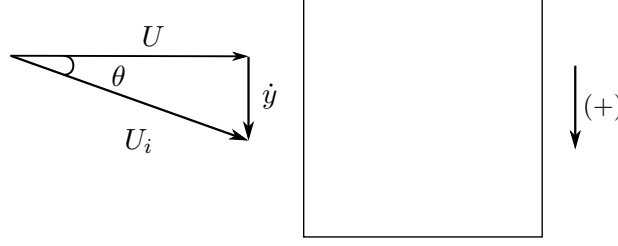


Figure 1.1: Induced angle of attack on the square prism due to the resultant of free-stream velocity of the fluid and transverse velocity of the body.

oscillating system (i.e. a simple spring, mass and damper system), the induced lift becomes the periodic forcing of the system. Galloping is sustained if the induced lift is in phase with the motion of the body. This could be explained further by using a square cross section as an example.

Figure 1.1 illustrates the motion of the body at a given instantaneous time. The induced angle of attack is formed on the square cross section as a result of the free-stream velocity vector  $U$  and the transverse velocity vector of the body  $\dot{y}$ . Thus, a force is formed in phase with the motion of the body (square cross section). This mechanism could also be observed on other bodies which are prone to galloping. The sign convention in this figure (and generally used in this scope of research) states that downward direction is positive. Hence, the force generated on a body under the influence of galloping, could be also identified as a “negative lift”.

### 1.2.2 Quasi-steady state theory

According Païdoussis et al. (2010), the initial studies by Glauert (1919) provided a criterion for galloping by considering the auto-rotation of a stalled aerofoil. As this phenomenon commonly occur in iced transmission lines, Den Hartog (1956) has provided a theoretical explanation for iced electric transmission lines.

The pioneering study in order to mathematically model galloping was conducted by Parkinson and Smith (1964). This model has been widely used in almost all subsequent studies regarding galloping. A weakly non-linear oscillator model was developed by them to predict the response of the system. Essentially the quasi-steady assumption was made to develop this theory assuming that the instantaneous induced lift force of the oscillating

body is equal to that of the lift force generated by the same body at the same induced angle of attack. In order to satisfy the quasi-steady assumption few conditions had to be satisfied.

- The velocity of the body does not change rapidly
- There is no interaction between vortex shedding and galloping

The second condition is satisfied by ensuring the vortex shedding frequency is much higher than the galloping frequency. The oscillator equation was solved using the Krylov and Bogoliubov method. Details of this method would not be mentioned as it is not used in the present study to solve the oscillator equation. The results obtained from experiments, carried out at  $Re = 2200$  and a mass ratio ( $m^*$ ) around 1164 had a good agreement with the theoretical data which is shown in figure 1.2.

### Quasi-steady state oscillator model

The equation of motion of transversely oscillating body is given by

$$m\ddot{y} + c\dot{y} + ky = F_y, \quad (1.1)$$

where the forcing term  $F_y$  is given by

$$F_y = \frac{1}{2}\rho U^2 \mathcal{A} C_y. \quad (1.2)$$

As explained previously, when quasi-steady assumption is used the stationary  $C_y$  data (which consists of both lift and drag data) of the body could be used as inputs to the oscillator equation. Parkinson and Smith (1964) used a 7<sup>th</sup> order odd interpolating polynomial to determine  $C_y$ . The order of the polynomial can be chosen arbitrarily depending on the study. For example Barrero-Gil et al. (2009, 2010) have used a 3<sup>rd</sup> order polynomial in order to simplify the analytical model. However, Ng et al. (2005) pointed out that a 7<sup>th</sup> order polynomial is sufficient as it does not provide a significantly better result.

$$C_y(\theta) = a_1 \left( \frac{\dot{y}}{U} \right) - a_3 \left( \frac{\dot{y}}{U} \right)^3 + a_5 \left( \frac{\dot{y}}{U} \right)^5 - a_7 \left( \frac{\dot{y}}{U} \right)^7. \quad (1.3)$$

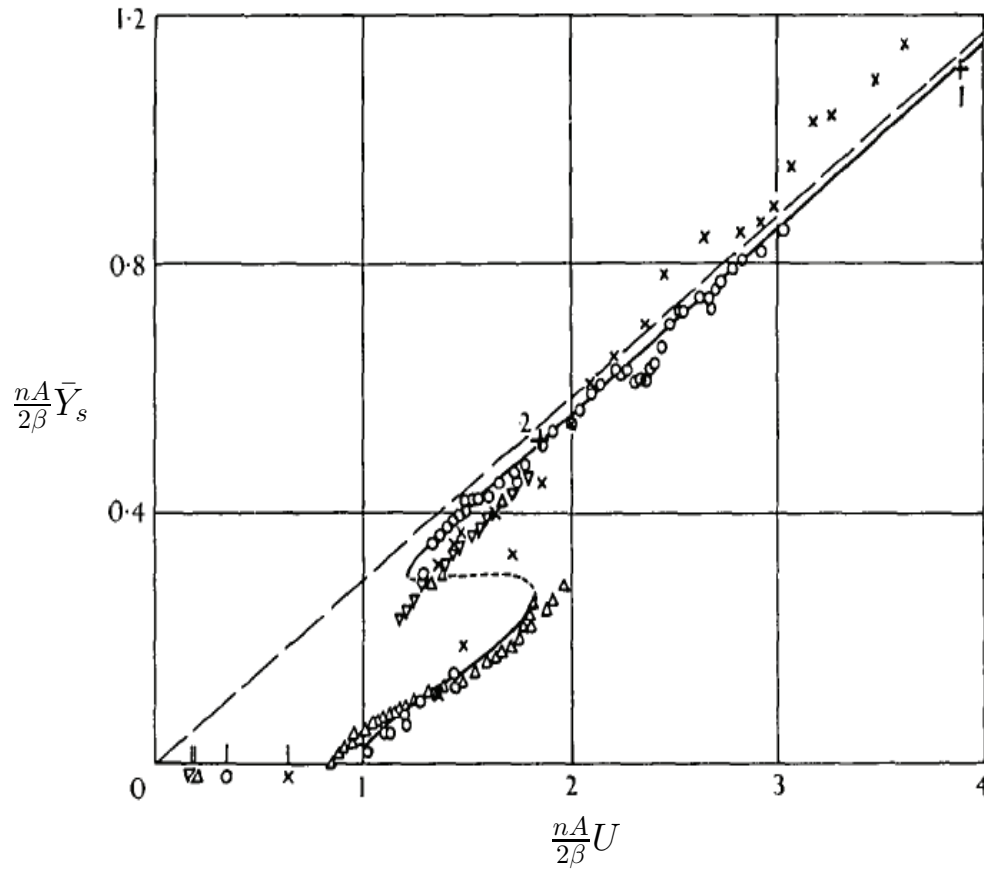


Figure 1.2: “Collapsed amplitude-velocity characteristic. Theory: ——— stable limit cycle, - - - unstable limit cycle. Experiment  $\times \beta = .00107$ ,  $\circ \beta = .00196$ ,  $\triangle \beta = .00364$ ,  $\nabla \beta = .00372$ ,  $+1 \beta = .0012$ ,  $+2 \beta = .0032$  Reynolds numbers 4,000 – 20,000 ”. Figure extracted from Parkinson and Smith (1964).  $\frac{nA}{2\beta}\bar{Y}_s$  is the dimensionless displacement amplitude parameter and  $\frac{nA}{2\beta}U$  is the reduced velocity.

Therefore by substituting the forcing function to the oscillator equation (Eq:1.1) the Quasi-steady state (QSS) model could be obtained (Eq:1.4).

$$m\ddot{y} + c\dot{y} + ky = \frac{1}{2}\rho U^2 \mathcal{A} \left( a_1 \left( \frac{\dot{y}}{U} \right) - a_3 \left( \frac{\dot{y}}{U} \right)^3 + a_5 \left( \frac{\dot{y}}{U} \right)^5 - a_7 \left( \frac{\dot{y}}{U} \right)^7 \right). \quad (1.4)$$

As the current study is focused on the low  $Re$  region, it is a known fact that the vortex shedding will be correlated well and therefore provide a significant forcing in the low Reynolds number region. Joly et al. (2012) introduced an additional sinusoidal forcing function to the model in order to integrate the forcing by vortex shedding. By the addition of this forcing Joly et al. (2012) managed to obtain accurate predictions of the displacement amplitude even at low mass ratios, where the galloping is suppressed or not present. Yet, the strength or the amplitude of this sinusoidal forcing has to be tuned in an *ad hoc* manner, and it was not clear the relationship between this forcing with the other system parameters. Thus in the current study this forcing was not used.

### Presence of hysteresis

Hysteresis could be observed in the amplitude data of Parkinson and Smith (1964). In contrast, the studies carried out by Barrero-Gil et al. (2009) and Joly et al. (2012) at much lower Reynolds numbers ( $159 \leq Re \leq 200$ ), did not show any hysteresis. Luo et al. (2003) concluded that the hysteresis was present due to the presence of an inflection point in the  $C_y$  curve at high Reynolds numbers (Parkinson and Smith (1964) data) which was not present at lower Reynolds numbers. It was further explained and demonstrated by Luo that the inflection point occurs due to the intermittent re attachment of the shear layer in certain angles at high Reynolds numbers.

### 1.2.3 Induced force and the shear layers

It is important to have an understanding on how the induced lift is generated in a fluid dynamics point of view. The quasi-steady model has already been validated and re-validated by many studies, therefore the flow-field data of static body simulations could be used to analyse the underpinning fluid dynamic mechanisms governing galloping.

The governing mechanism of galloping is the behaviour of the shear layers created at the leading edge due to flow separation on the top and bottom of the body. A common

## 1. A REVIEW OF THE LITERATURE

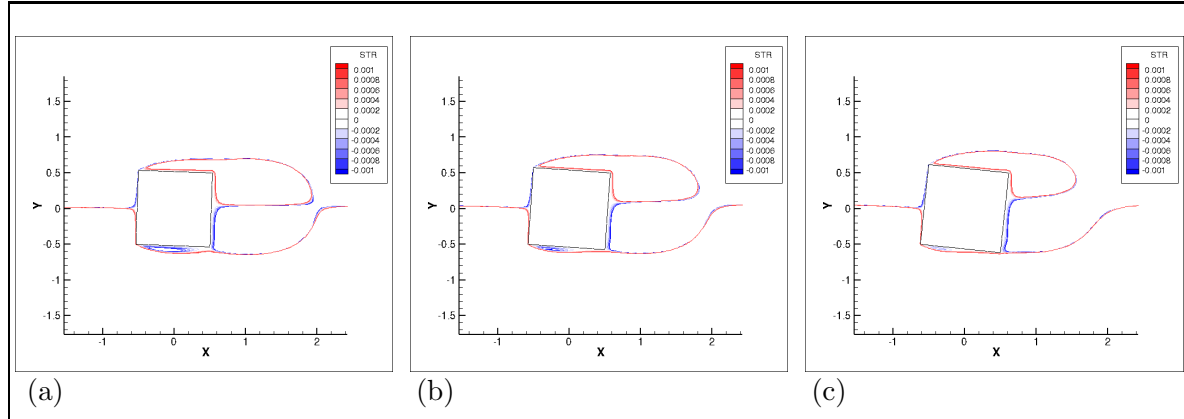


Figure 1.3: Stream functions of time averaged flow field on a stationary square section at  $Re = 200$  at different incidence angles. (a)  $2^\circ$  ( $C_y$  increases), (b)  $4^\circ$  ( $C_y$  peaks) and (c)  $2^\circ$  ( $C_y$  decreases). The bottom shear layer comes closer to the bottom wall and reattaches as the angle of incidence increase.

example is a square cross section which has been used widely in studies on galloping. In this square cross section (figure 1.3) the flow separate from the leading edges of the body and create two shear layers on the top and bottom sides of the the body. Figure 1.3 shows the stream functions of time averaged (over a vortex shedding cycle) flow fields of stationary cross sections. The angle of incidence increases clockwise from  $2^\circ - 6^\circ$ . As  $\theta$  is increased, the bottom shear comes closer to the wall of the body compared to the top shear layer (Figure 1.3 (a)). The shear layer nearer to the body crates higher suction compared to the shear layer at the opposite side. This pressure imbalance between the top and bottom sides of the body creates a downward force (i.e. the negative lift). As the angle is increased, the bottom shear layer becomes more closer and therefore the pressure difference becomes grater leading to a higher  $C_y$ . The negative lift force becomes maximum when the shear layer near to the wall reattaches at the trailing edge (figure 1.3 (b)). As  $\theta$  is further increased, the bubble in the bottom shear layer shrinks in size resulting the reduction of the pressure imbalance of the top and bottom surface leading to the reduction in  $C_y$ . put the cY curve as crodd reference. As the body is connected to an oscillatory system (discussed in section 1.2.1), this shear layer behaviour also harmonize with the cyclic behaviour of the system providing the driving force to the system so that the motion of galloping is sustained.



### 1.2.4 Frequency response

It is clear that the cyclic motion of the shear layer harmonize with the mechanical system. Therefore, the frequency response should be then, the natural frequency of the system  $\omega_n$  which much is different from VIV mechanism, where the primary frequency comes from the periodic forcing of the vortex shedding. Hence, in the QSS model the natural frequency of the system could be identified as the frequency of oscillations. However, it should be noted that this is valid on the regimes where the conditions discussed in section 1.2.2 are satisfied.

On the other hand, the forcing function in the QSS model equation 1.4, is a non linear function. As the mass ratio is quite high, the non-linearities of the forcing does not make much effect to the frequency response. However, as the mass ratio goes down theoretically the non linearities of the forcing should affect the frequency response of the system.

The experimental studies carried by Bouclin (1977) concluded at high reduced velocities with large inertia, the motion of the cylinder controls the frequency of the system rather than the vortex shedding. The structural damping has no effect provided that it is small. He also concluded that as the inertia and the reduced velocity gets lower, there is some interaction between vortex shedding and galloping. And at this region the frequency is mainly governed by the vortex shedding.

### 1.2.5 Fluid mechanics governing the galloping response

As discussed in subsection 1.2.3 the driving force of a galloping system is the asymmetrical placement of the shear layers at either sides of the body. In consequence, it is clear that a significant afterbody is needed for the shear layer interaction to sustain galloping. Parkinson (1974, 1989) and Bearman et al. (1987) have discussed well the importance of the length and the shape for galling in their reviews. It is also highlighted in Parkinson (1974) that the most important physical parameters for galloping are the size relative to the characteristic hight and the shape of the afterbody. Manipulating the shape of the afterbody and thereby, manipulating the shear layer interactions with the body, gives the ability to control the galloping response. Thus, due to this reason work has been carried out on the response of galloping of different cross sectional shapes.

Blevins (1990) provided a good comparison of the shapes which are prone to galloping based on the work by Parkinson and Brooks (1961), Nakamura and Mizota (1975) and Nakamura and Tomonari (1977). The reproduction of Blevins's data could be found in Païdoussis et al. (2010) presented in figure 1.4.

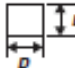
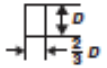


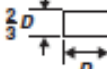
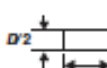
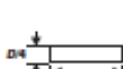
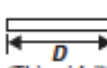

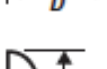

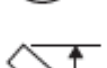
Naudascher and Wang (1993), Ruscheweyh et al. (1996), Deniz (1997) and Weaver and Veljkovic (2005) are some of the work done on different cross sectional shapes. Alonso et al. (2009) carried out wind tunnel tests on biconvex and rhomboidal cross sections. Studies were further carried out by Alonso for elliptical cross sections (Alonso et al., 2010) and triangular cross sections (Alonso et al., 2005). The regions of stability for galloping at different angles of attack and the static force coefficients are presented in these studies with regards to the cross section involved.

### 1.2.6 Galloping as a mechanism of energy harvesting

The focus on fluid-elastic galloping in the past was on understanding and developing methods to suppress it, due to the adverse effects on civil structures. However, recently, the focus of research has been redirected to develop mechanisms to excite galloping rather than suppressing it. This is due to the recent trend on the search of alternate energy sources with minimal environmental impact have lead researchers working on investigating the possibility of extracting useful energy from flow induced vibrations.

Bernitsas and his group in the University of Michigan have made significant progress on using VIV as potential candidate for energy extraction. Bernitsas et al. (2008) introduced the concept of using VIV as a mode of energy extraction. The group have developed a device called VIVACE converter based on this concept. The work has been further expanded to focus on various aspects (such as Reynolds number effects, damping effects etc.) in Bernitsas et al. (2009); Raghavan et al. (2009); Raghavan and Bernitsas (2011); Lee et al. (2011).

To this end, investigations on the possibility of using fluid-elastic galloping as a mode of energy extraction have not being pursued much. Barrero-Gil et al. (2010) was the first work which placed the concept of using fluid-elastic galloping as a mode of energy harvesting. In his paper Barrero-Gil et al. (2010) clearly explains the advantages of using galloping as a mode of energy harvesting. Unlike VIV, galloping is not a resonant phenomenon which

Section	$h/d$	$\partial C_{Fy}/\partial \alpha$		Reynolds number
		Smooth flow	Turbulent flow <sup>b</sup>	
	1	3.0	3.5	$10^5$
	3/2	0.	-0.7	$10^5$
	2	-0.5	0.2	$10^5$
	4	-0.15	0.	$10^5$
	2/3	1.3	1.2	$6.6 \times 10^4$
	1/2	2.8	-2.0	$3.3 \times 10^4$
	1/4	-10.	-	$2 \times 10^3 - 2 \times 10^4$
 (Thin airfoil)	- <sup>c</sup>	-6.3	-6.3	$> 10^3$
	-	-6.3	-6.3	$> 10^3$
	-	-0.1	0.	$6.6 \times 10^4$
	-	-0.5	2.9	$5.1 \times 10^4$
	-	0.66	-	$7.5 \times 10^4$

<sup>a</sup>  $\alpha$  is in radians; flow is left to right.  $\partial C_{Fy}/\partial \alpha = -\partial C_{Ll}/\partial \alpha - C_D$ , with  $C_{Fy}$  based on the dimension  $D$ , so that  $\partial C_{Fy}/\partial \alpha > 0$  for galloping.

<sup>b</sup> Approximately 10% turbulence.

<sup>c</sup> Inappropriate to use  $h/d$ .

Figure 1.4: “The transverse force coefficient for various sections in steady smooth or turbulent flow (after Blevins (1990))” obtained from Païdoussis et al. (2010)

## 1. A REVIEW OF THE LITERATURE

---

needs the synchronisation or “lock-in” and therefore have the following advantages.

- The range where significant oscillations develop is not restricted to a narrow band of frequencies.
- Galloping does not have a self-limited response beyond the critical velocity (Barrero-Gil et al., 2010) and therefore the amplitudes increase as the flow velocity is increased.

## CHAPTER 2

---

# METHODOLOGY AND VALIDATION

### 2.1 Introduction

A brief overview of the computational methods to perform the simulations to obtain the data in this thesis are presented in this chapter. As the this particular study is not focused on developing computational methods but concentrated on understanding the physics of a body under the influence of fluid-elastic galloping, it should be noted that the overview provided in this chapter is quite abstract.

The flow of this chapter is as follows. First the equations used to model the system are presented and

Finally, a series of validation data are presented and discussed to ensure the accuracy of the direct numerical simulations in order to ensure the confidence in the numerical predictions of this thesis.

#### 2.1.1 Parameters used

The data in this project are mainly presented in two categories, high and low Reynolds numbers to compare results at laminar and turbulent range. One main objectives in this study was to capture the flow physics accurately using direct numerical simulations hence, major portion of the study was carried out in the laminar range where the flow is close to 2D. Although majority of data are focused on low Reynolds numbers, some data were presented using inputs from high Reynolds numbers to the QSS model to provide a comparison between high and low Reynolds numbers.  $Re = 200$  was defined as the “low” Reynolds

number and  $Re = 22300$  was defined as the high Reynolds number. Studies by Tong et al. (2008) and Sheard et al. (2009) reveals that the approximate value of 3-dimensional transition of the wake for a square cross section is  $Re = 160$  and therefore,  $Re = 200$  was selected to represent the low Reynolds number regime, also considering the fact that other numerical studies in the laminar regime have used this value for the Reynolds number (Robertson et al., 2003; Joly et al., 2012). The reason behind considering the flow regimes of a square cross section was the fact that the basic cross section being used in this study was a square. The selection of the value for the high Reynolds number was fairly simple as it was the Reynolds number where the pioneering study of galloping Parkinson and Smith (1964) provided the experimental input data ( $C_y data$ ) for the QSS model.

Stationary  $C_y$  data at different angles of attack to be used as inputs to the QSS model, were obtained for the low Reynolds number regime using direct numerical simulations. The average power was obtained by using equation ??, and the averaging was done over no less than 20 galloping periods. For the high  $Re$  tests, predictions of power output at  $Re = 22300$  were obtained using the coefficients for the  $C_y$  curve from Parkinson and Smith (1964). The mass ratio  $m^*$  was kept at 1163 for  $Re = 22300$  (Similar to Parkinson and Smith (1964)),  $m^* = 20$  for  $Re=200$  and  $U^* \geq 40$  similar to the parameters used in literature (Robertson et al., 2003; Joly et al., 2012) to obtain a comparison with published work. These parameters were used throughout this study unless otherwise specified.

### 2.2 Quasi-steady model

The quasi-steady state model discussed in section 1.2.2 was used to obtain oscillator response data. The quasi-steady state model has proven its ability to obtain accurate galloping response data (discussed in section 1.2.2). Therefore, it enables to obtain large number of at the expense of a short computational time. The oscillator equation consist of spring, mass and damper oscillator expression with a 7<sup>th</sup> order interpolation polynomial as the forcing function (equation 1.4).

### Solving the quasi-steady state equation

The quasi-steady model being an ordinary differential equation could be solved using different solving methods. Some of the techniques include limit cycle oscillations, harmonic balance, cell mapping and numerical integration. Vio et al. (2007) showed that numerical integration provides accurate data. A fourth-order Runge-Kutta ODE solving scheme was used in solving the quasi-steady state oscillator equation. The built in ‘ode45’ function in MATLAB was used primarily to solve the QSS equation while in some cases ‘ode15s’ function was used when the equation became more stiff.

## 2.3 Calculation of average power

The ideal potential amount of harvested power output could be represented as the dissipated power due to mechanical damping before losses in any power take-off system are included. Thus the mean power output could be expressed as

$$P_m = \frac{1}{T} \int_0^T (c\dot{y})\dot{y}dt, \quad (2.1)$$

where  $T$  is the period of integration and  $c$  is the mechanical damping constant.

The work done on the body by the fluid is equal to this quantity, defined as

$$P_m = \frac{1}{T} \int_0^T F_y \dot{y}dt, \quad (2.2)$$

where  $F_y$  is the transverse (lift) force.

The two definitions of the mean power provide two vital interpretations of power transfer. Equation ?? shows that the power is proportional to the mechanical damping and the magnitude of the transverse velocity. At first glance one may assume that the power could be increased by increasing damping. In a practical power extraction device, the significant component of damping would be due to the electrical generator and therefore, an increase in damping would be due to the increase of the load or in other words the electrical resistance. Yet this perception of damping is not quite accurate as very high damping would result in reducing the velocity amplitude which then, would not result in a higher energy output according to equation ?. In consequence, a balance need to be obtained where the

damping is high, but not to the extent that it will adversely result by overly suppressing the motion of the body.

On the other hand, equation ?? shows that a higher power is attained during situations where the transverse force  $F_y$  and the transverse velocity are in phase. Hence, a simple increase in the magnitude of the force or the velocity is not satisfactory to attain a higher power transfer. Any increase in magnitude of either of the parameters (force or velocity) is linked to an increase in phase.

### 2.4 Direct numerical simulations (DNS)

Direct numerical simulations were employed to obtain the stationary data to be used as inputs to the QSS model and to obtain fluid-structure interaction (FSI) data to be compared with the QSS model at low Reynolds numbers. A high-order in-house build spectral element which simulates two-dimensional laminar flows was used to obtain the DNS data.

To obtain DNS results an in-house build code was used. This code essentially solves the Navier-Stokes equations in an accelerated reference frame. A three-step time-splitting scheme also known as a fractional step method was used for temporal discretisation. A predictor-corrector method was used for the FSI data where an elastically mounted body was involved. A description of the spectral element method in general can be found in Karniadakis and Sherwin (2005). This code has been very well validated in a variety of fluid-structure interaction problems similar to that studied in the current study (Leontini et al., 2007; Griffith et al., 2011; Leontini et al., 2011; Leontini and Thompson, 2013). A overview of the algorithm is presented in the following subsections.

#### 2.4.1 Governing equations

Assumptions have to be made in any numerical simulation. In this study, the following key assumptions were made to carry out the direct numerical simulations.

To formulate the differential equations to an infinitesimally small fluid section, the fluid was assumed to be continuum. This assumption is valid for all macro flows. However, it the validity of this assumptions as the fluid dynamics involved reduces to micro and nano scale as the lengths scales involved approaches length scales of the molecules.



Next, To avoid the consideration of acoustic wave propagation it was assumed that the density of the fluid is constant hence, the fluid is incompressible. This particular assumption is valid for Mach numbers (ratio of the speed of sound to the speed of fluid flow ) less than 0.3. In order to disregard the density gradients the fluid was assumed to be isothermal.

Finally, the fluid was assumed to be an Newtonian fluid, which means that the shear stress is directly proportional to the strain rate.

These assumptions are quite standard and further information could be found in White (1999).

The Naiver-Stokes equations are the equations which describes a Newtonian, incompressible contentious fluid.

$$\frac{\partial \mathbf{u}}{\partial t} + (\mathbf{u} \cdot \nabla) \mathbf{u} = -\frac{\nabla p_f}{\rho} + \frac{\mu_v}{\rho} (\nabla^2 \mathbf{u}) , \quad (2.3)$$

and continuity,

$$\nabla \cdot \mathbf{u} = 0 . \quad (2.4)$$

The velocity vector filed is represented by  $\mathbf{u}$ , time variable by  $t$ , the pressure field by  $p_f$  fluid density by  $\rho$  and the dynamic or kinematic viscosity by  $\mu_v$ . In the Naiver-stokes equation (2.3) the left hand side represents the inertial forces and the right hand side represents the pressure forces. The net mass flux into the fluid element is specified to be zero by the continuity equation.

These equations are generalised by non-dimensionalisation. In the case of bluff body wake flows, the equations are non-dimensionalised by using the characteristic length of the body i.e the frontal projected hight  $D$ , and the free-stream velocity  $U$ .

The equations are modified to be solved in an accelerated reference frame in this particular study where the frame of reference is attached to the cylinder. Therefore, an extra term is added to the Naiver-stokes equations which the acceleration of the cylinder. Thus, the equations could be written as,

$$\frac{\partial \mathbf{V}}{\partial \tau} = -\nabla P + \frac{1}{Re} (\nabla^2 \mathbf{V}) - (\mathbf{V} \cdot \nabla) \mathbf{V} + \frac{d\mathbf{V}_{cyl}}{d\tau} , \quad (2.5)$$

$$\nabla \cdot \mathbf{V} = 0 . \quad (2.6)$$

$\mathbf{V} = \mathbf{u}/U$ ,  $\tau = tU/D$ ,  $P = p_f/(\rho U^2)$ ,  $Re = \rho U D/(\mu_v)$ ,  $\mathbf{V}_{cyl} = \mathbf{v}_{cyl}/U$ , and  $\mathbf{v}_{cyl}$  being the velocity of the cylinder.  $\frac{d\mathbf{V}_{cyl}}{d\tau}$ , represents acceleration term.

The Naiver-Stokes equations are coupled by with the oscillator differential equation

$$\frac{\ddot{y}_{cyl}}{D} + 2\zeta\sqrt{k^*}\frac{\dot{y}_{cyl}}{D} + k^*\frac{y_{cyl}}{D} = \frac{\pi}{2}\frac{C_L}{m^*}, \quad (2.7)$$

$\zeta$  is the damping ratio,  $k^* = kD^2/mU^2$  and  $C_L = F_{lift}/(0.5\rho U^2 D)$ . The lift coefficient per unit length of the body is  $C_L$ , the transverse displacement of the cylinder is given by  $y_{cyl}$ , the characteristic length scale of the body is  $D$ ,  $k$  is the spring constant and the mass per unit length of the body is represented by  $m$ . The general form of this linear oscillator equation could be found in books such as ?. The final form of the coefficients were constructed by non-dimensionalising the general from of the oscillator equation.

### 2.4.2 Temporal discretisation:Time-splitting

The problem was discretised in order to solve equations 2.5, 2.6 and 2.7 in both space and time. A three-step time splitting method was used for the temporal discretisation. This scheme also known as the fractional step method, was used to separately integrate the terms in the right hand side of the Naiver-Stokes equation. The overall integration of one time-step is split into three substeps. An approximate solution of the Naiver-Stokes equation is gained by this scheme.

The cylinder acceleration is integrated through the whole time step in order to obtain a initial approximation of the intermediate velocity filed. This velocity filed is used as the stating condition. The pressure is integrated using this starting condition. A secondary intermediate velocity filed is obtained as a result of the pressure integration substep. This secondary velocity filed is then used as the starting condition for the integration of the diffusion of term which results in the final velocity filed.

The three semi-discretised substep equations are as follows:

$$\mathbf{V}^* - \mathbf{V}^{(n)} - \Delta \mathbf{V}_{cyl} = - \int_{\tau}^{\tau+\Delta\tau} (\mathbf{V} \cdot \nabla) \mathbf{V} d\tau \quad (2.8)$$

$$\mathbf{V}^{**} - \mathbf{V}^* = - \int_{\tau}^{\tau+\Delta\tau} \nabla P d\tau \quad (2.9)$$

$$\mathbf{V}^{(n+1)} - \mathbf{V}^{**} = \frac{1}{Re} \int_{\tau}^{\tau+\Delta\tau} \nabla^2 \mathbf{V} d\tau, \quad (2.10)$$

The current time step is represented by  $n$  and the intermediate velocity fields at the end the convection and pressure substeps are  $\mathbf{V}^*$  and  $\mathbf{V}^{**}$  respectively. The change in the body over a time step is given by  $\Delta \mathbf{V}_{cyl} = \int_{\tau}^{\tau+\Delta\tau} \frac{d\mathbf{V}_{cyl}}{d\tau} d\tau$ .

The addition of these three substep equations reduces to the integrated form of the Naiver-Stokes equation in equation 2.5.

### Integration of the substep equations

The integration methods of the pressure, convection and diffusion substeps are presented in this subsection.

#### The convection substep

As the system has a free oscillation, a coupling between the oscillation equation (equation 2.7) and the Naiver-Stokes equations had to be employed. As a result, the cylinder dynamics had to be solved at each time-step.

An iterative predictor-corrector scheme was employed to obtain the solution of the coupled equations. The initial step being the “predictor” step was obtaining approximations for all the quantities involved in the integration. A quadratic extrapolation was used to obtain an initial estimate of  $\Delta \mathbf{V}_{cyl}$  from three previous time step values of  $\mathbf{V}_{cyl}$ . Therefore, a non-dynamical approximation could be obtained.

$$\mathbf{V}_{cyl}^{(n+1)\dagger} = 3\mathbf{V}_{cyl}^{(n)} - 3\mathbf{V}_{cyl}^{(n-1)} + \mathbf{V}_{cyl}^{(n-2)}, \quad (2.11)$$

The dagger ( $\dagger$ ) represents that the value is an initial approximation eg.  $\mathbf{V}_{cyl}^{(n+1)\dagger}$ . Thus,  $\Delta \mathbf{V}_{cyl}^\dagger$  was obtained by a simple subtraction of the value at the current time step.

The approximated position of the cylinder at the next time step could be obtained by carrying out an integration of the cylinder velocity over the time step. A third-order Adams-Moulton method was used to perform the integration. Therefore, the final equation describing the position of the body is given by,

$$\frac{y_{cyl}^{(n+1)\dagger} - y_{cyl}^{(n)}}{\Delta\tau} = \frac{1}{12}(5\mathbf{V}_{cyl}^{(n+1)\dagger} + 8\mathbf{V}_{cyl}^{(n)} - \quad (2.12)$$

The transverse displacement of the cylinder is denoted by  $y_{cyl}$ , and the dagger denotes the initial approximation.

## 2. METHODOLOGY AND VALIDATION

---

An offset is present between the cylinder velocity and cylinder position. The velocity of the cylinder is in advance by half a time-step of the position of the cylinder which is  $\mathbf{V}_{cyl}^{(n+1)}$  is half a time step is in advance of  $y_{cyl}^{(n+1)}$ . However, both the cylinder positions and the velocities are located at the same discrete times.

In order to obtain an approximation for  $\mathbf{V}^*$ , a solution was obtained for equation 2.8 using the previous approximated quantities.

By using a third-order Adams-Bashforth scheme and incorporating the approximation of equation 2.11 for  $\Delta\mathbf{V}_{cyl}^\dagger$  the first approximation for  $\mathbf{V}^*$  was obtained using the equation,

$$\frac{\mathbf{V}^* - \mathbf{V}^{(n)} - \Delta\mathbf{V}_{cyl}^\dagger}{\Delta\tau} = \frac{1}{12}(23\mathbf{N}(\mathbf{V})^{(n)} - 16\mathbf{N}(\mathbf{V})^{(n-1)} + 5\mathbf{N}(\mathbf{V})^{(n-2)}) . \quad (2.13)$$

The explicit integration method was only used for the first approximation and for the subsequent iterations semi-implicit method was used for  $\mathbf{V}^*$ .

This step was followed by solving the remaining substep equations in order to obtain an approximation for  $\mathbf{V}^{(n+1)\dagger}$ , and then the ‘‘predictor’’ portion of the predictor-corrector method was completed.

The cylinder velocity approximation  $\mathbf{V}_{cyl}^\dagger$ , was updated commencing the ‘‘corrector’’ cycle of the predictor-corrector method. This was carried out using a third-order integration scheme.

$$\frac{\mathbf{V}_{cyl}^{(n+1)\dagger} - \mathbf{V}_{cyl}^{(n)}}{\Delta\tau} = \frac{1}{24}(25\ddot{y}_{cyl}^{(n+1)} - 2\ddot{y}_{cyl}^{(n)} + \ddot{y}_{cyl}^{(n-1)}) . \quad (2.14)$$

$\Delta\mathbf{V}_{cyl}^\dagger$  was updated using the recalculated value of  $\mathbf{V}_{cyl}^{(n+1)\dagger}$ . The velocity was integrated over a time step in order to obtain the position of the cylinder. For the first correction cycle a third order Adams-Moulton method was used which completed the first iteration of the predictor-corrector method.

$$\frac{y^{(n+1)\dagger} - y^{(n)}}{\Delta\tau} = \frac{1}{12}(5\mathbf{V}_{cyl}^{(n+1)\dagger} + 8\mathbf{V}_{cyl}^{(n)} - \mathbf{V}_{cyl}^{(n-1)}) , \quad (2.15)$$

Slight modifications were employed to the subsequent iterations in order to improve numerical stability however, the iterations proceeded in a similar manner. As the approximations for  $\Delta\mathbf{V}_{cyl}^\dagger$  and  $\mathbf{V}^{(n+1)\dagger}$  were available, using third-order Adams-Moulton scheme further correction steps were employed.

$$\frac{\mathbf{V}^* - \mathbf{V}^{(n)} - \Delta \mathbf{V}_{cyl}^\dagger}{\Delta \tau} = \frac{1}{12}(5\mathbf{N}(\mathbf{V})^{(n+1)\dagger} + 8\mathbf{N}(\mathbf{V})^{(n)} - \mathbf{N}(\mathbf{V})^{(n-1)}) . \quad (2.16)$$

The two remaining substeps were then solved to obtain a new approximation of  $\mathbf{V}^{(n+1)\dagger}$ .

The first correction step was carried out by employing 2.14 to obtain a second estimate for the velocity of the cylinder  $\mathbf{V}_{cyl}^{(n+1)\ddagger}$ . A relaxation equation (equation 2.17) was used for the velocity of the cylinder prior to using equation 2.15 since the equations were quite stiff.

$$\mathbf{V}_{cyl}^{(n+1)'} = \mathbf{V}_{cyl}^{(n+1)\dagger} + \epsilon(\mathbf{V}_{cyl}^{(n+1)\ddagger} - \mathbf{V}_{cyl}^{(n+1)\dagger}) , \quad (2.17)$$

$\mathbf{V}_{cyl}^{(n+1)\ddagger}$  and  $\mathbf{V}_{cyl}^{(n+1)\dagger}$  represent the most current and previous approximations respectively. The under relaxation parameter is represented by  $\epsilon$  which controls the proportion of the correction which is considered in each iteration. The final approximation at the end of the relaxation process is represented by  $\mathbf{V}_{cyl}^{(n+1)'}$  was used in equation 2.15 in the completing the correction cycle and hence, the iteration.

A convergence error criteria was given until which the iteration was continued. The lift force of the cylinder, the velocity of the cylinder and the fluid velocity should all converge to the required convergence criteria. A series of convergence studies were carried out in order to obtain the convergence criteria (Pregalato, 2003). The solution converged within 3 – 4 iterations and the iteration count exceeded 10 in very rare cases.

The procedure to obtain the solution for  $\mathbf{V}^*$  (velocity filed at the end of the convection substep) in a nutshell is as follows. A predictor-corrector method was employed, where the primary predictor cycle was first employed. This was followed by obtaining an approximation for  $\Delta \mathbf{V}_{cyl}$  which was calculated using equation 2.11. From this approximation ( $\Delta \mathbf{V}_{cyl}$ ) the position of the cylinder was approximated using equation 2.12.

Next, using an explicit Adams-Bashforth scheme, an approximation was obtained for  $\mathbf{V}^*$  by solving the substep equation (equation 2.13). The predictor cycle was completed by solving the remaining substep equations to arrive at the first approximation of  $\mathbf{V}^{(n+1)}$ .

Then, the primary corrector step was initiated by calculating the forces of the body from the current approximation of  $\mathbf{V}^{(n+1)}$ . Using these forces together with the current approximations of the velocity and the displacement of the body and the equation of motion of the body (eq:2.7) an approximation for the acceleration of the cylinder at the end of the timestep was obtained. By integrating this acceleration over the timestep using equation

## 2. METHODOLOGY AND VALIDATION

---

2.14 the corrected approximation of  $\Delta \mathbf{V}_{cyl}$  was obtained. Using equation 2.15 the corrected approximation for  $y_{cyl}^{(n+1)}$  was obtained by integrating the velocity over a timestep by using the recent value of  $\Delta \mathbf{V}_{cyl}$ . The primary corrector step and the primary iteration was completed once this step was completed. All the remaining iterations were carried out in a similar manner by with a under relaxation presented in equation 2.17.

### The pressure substep

The pressure equation was solved in two parts in order to find solutions the two unknowns i.e. the pressure filed and the velocity filed at the end of the timestep.

The integration of the pressure substep was initiated by formulating equation 2.9 in terms of a second-order Adams-Moulton scheme which gives,

$$\frac{\mathbf{V}^{**} - \mathbf{V}^*}{\Delta \tau} = -\frac{1}{2}(\nabla P^{(n+1)} + \nabla P^{(n)}) . \quad (2.18)$$

The equation was further reduced by considering that the *RHS* is equal to  $\nabla P^{(n+1/2)}$ . The divergence portion of equation 2.18 was taken. Using equation 2.6, continuity was applied to the velocity filed which resulted the pressure filed having a Poisson equation of the form of

$$\nabla^2 P^{(n+\frac{1}{2})} = \frac{1}{\Delta \tau} \nabla \cdot \mathbf{V}^* . \quad (2.19)$$

This equation could be solved at the middle of the timestep for the pressure filed. Therefore, this pressure filed could then be back-substituted to equation 2.18, together with the simplified *RHS*, to solve for the velocity filed  $\mathbf{V}^{**}$ , at the end of the substep.

### The diffusion substep

A numerical stability of the solution scheme has to be considered for the diffusion substep although the equation for diffusion was linear. Therefore, the Crank-Nicholson scheme or the second order Adams-Moulton scheme which is a semi-implicit scheme which is also unconditionally numerically stable. Thus this formulates the final equation (eq 2.10) of the time splitting scheme as,

$$\frac{\mathbf{V}^{(n+1)} - \mathbf{V}^{**}}{\Delta\tau} = \frac{1}{2Re}(\nabla^2 \mathbf{V}^{(n+1)} + \nabla^2 \mathbf{V}^{(n)}) . \quad (2.20)$$

The integration over the timestep is completed from the solution of this equation for  $\mathbf{V}^{(n+1)}$ , thus completing the time splitting scheme.

### Special discretisation:Spectral element method

The spacial discretisation was done using a nodal based spectral-element method. This method is a member of the finite-element class. The computational domain is separated into a series of macro elements and then a continuous solution is obtained over each element. Mesh refinement can be done in the areas where high gradients are experienced, which is also known as  $h$ -refinement. It was necessary that all elements to be quadrilateral. Yet, the elements were not restricted having curved sides.

The calculation of the residual  $\mathbf{R}$ initials the solution process. All the terms of the governing equations (the Naiver-Stokes equation eq 2.5) were moved to the *LHS*. Thus, the resulting expression is,

$$\frac{\partial \mathbf{V}}{\partial \tau} + \nabla P - \frac{1}{Re}(\nabla^2 \mathbf{V}) + (\mathbf{V} \cdot \nabla) \mathbf{V} - \frac{d\mathbf{V}_{cyl}}{d\tau} = 0 . \quad (2.21)$$

A trial solution is substituted into the equation 2.21. The *RHS* of the equation would be zero if the trial solution is exact solution of the equation. If the trial solution is not the exact solution but an approximation to the exact solution which is the case in general, then the *RHS* will be non-zero and a residual will be formed. This residual could be defined by,

$$\frac{\partial \mathbf{V}_{trial}}{\partial \tau} + \nabla P_{trial} - \frac{1}{Re}(\nabla^2 \mathbf{V}_{trial}) + (\mathbf{V}_{trial} \cdot \nabla) \mathbf{V}_{trial} - \frac{d\mathbf{V}_{cyl}}{d\tau} = \mathbf{R} , \quad (2.22)$$

The trial solutions for velocity and pressure fields are  $\mathbf{V}_{trial}$  and  $P_{trial}$  respectively. The error term which is introduced through the trial function is the residual  $\mathbf{R}$ . It is clear from equation 2.22 that the definition of the residual is the governing equation substituted by the trial solution substituted to the true solution.

In order to effectively distribute the error over the domain, the residual has to be weighted in order to minimise the maximum local error. To perform this task the inner product of the residual with a series of weighing functions were taken. The integral of the

## 2. METHODOLOGY AND VALIDATION

---

product of the weighting function and the residual is the inner product of the residual which is set to zero. The method employed here is also commonly known as weighted residual methods.

Tensor-product Lagrange polynomials were used for both interpolating trial functions and weighting functions in the DNS carried out in this study. The order of the polynomials  $p$  could be varied from 2 to 14 in order to further improve grid resolution which is also known as  $p$  refinement. This  $p$  refinement coupled with  $h$  refinement leads to a method called  $h-p$  method which is used to improve accuracy (Karniadakis and Sherwin, 2005). The method also could be referred as a Galerkin method as both trial and weighting functions used were from the same family of functions. Fletcher (1984, 1991) provides further details on weighted-residual methods and Galerkin method.

Lagrange polynomials could be defined as,

$$L_i(\xi) = \prod_{\substack{g=1 \\ g \neq i}}^{p+1} \frac{(\xi - \xi_g)}{(\xi_i - \xi_g)} \quad (2.23)$$

The special coordinate is  $\xi$  and the indices of the data points are represented by  $i$  and  $g$  and the number of data points are represented by  $p + 1$ . One of the properties of Lagrange polynomials is that being equal to unity at the point  $i$  and being zero at all the other points other than in places in between points. Thus a continuous polynomial which matches the exact values of the velocity at the node point could be obtained when  $L_i$  is multiplied by the velocity at point  $i$  and then summing over all points. The tensor-product polynomials in two dimensions  $N_{q,s}(\xi, \eta)$  could be defined as the product of the Lagrange polynomial in one direction  $L_q(\xi)$ , with that in the other direction  $L_s(\eta)$ .

The outline of the procedure to find the solution is as follows. The process is initiated by forming inner product of the residual and the tensor-product Lagrange polynomial weighting function.

This gives the integral

$$\int \int_{\Omega} N_{k,m}(\xi, \eta) \cdot \left[ \frac{\partial \mathbf{V}_{trial}}{\partial \tau} + \nabla P_{trial} - \frac{1}{Re} (\nabla^2 \mathbf{V}_{trial}) + (\mathbf{V}_{trial} \cdot \nabla) \mathbf{V}_{trial} - \frac{d\mathbf{V}_{cyl}}{d\tau} \right] dx dy = 0, \quad (2.24)$$



The computational domain is represented by  $\Omega$ .  $N_{q,s}(\xi, \eta)$  which are the weighting function is defined in the computational space.

From equation 2.24 it is shown that each term in the equation is multiplied by the weighting function. Thus, the integral is split into components and the process could be carried out in the each of the substep equations 2.8, 2.9 and 2.10.

The first term in equation 2.13 could be used as an example to illustrate the process of obtaining the solution using the spectral element method. In order to calculate the integral of the equation ( use the appropriate equation ) over the entire computational domain, the integral is evaluated over each element separately. After that, the contributions of each element are summed together.

All the quadrilateral elements are mapped to a square ranging between  $-1, 1$  in both directions where  $\xi$  and  $\eta$  are the orthogonal coordinates of this square. The approximation of the integral is simplified by defining the internal node points with the Gauss-Lobatto-Legendre (GLL) quadrature.

A Jacobian is introduced to perform this coordinate transformation and hence, the integral over each element becomes,

$$\int \int_{El} \mathbf{V}^* N_{q,s}(\xi, \eta) \mathbf{J}(\xi, \eta) d\xi d\eta , \quad (2.25)$$

The Jacobian is represented by  $\mathbf{J}$  and  $El$  denotes that the integration is performed over a single element. The solution of equation 2.25  $\mathbf{V}_{trial}^*$ , could be re-written as a summation of Lagrange polynomial components. This equation also expresses the tensor-product Lagrange polynomials representing the weighting functions in directions of  $\xi$  and  $\eta$ . Therefore, the equation could be expressed as,

$$\int \int_{El} \sum_{i,j} \widehat{\mathbf{V}}^* L_i(\xi) L_j(\eta) L_q(\xi) L_s(\eta) \mathbf{J}(\xi, \eta) d\xi d\eta . \quad (2.26)$$

The velocity in the nodal points are represented by  $\widehat{\mathbf{V}}^*$ ,  $L$  is the one-dimensional Lagrange polynomial and  $i$  and  $j$  represents the node locations in directions  $\xi$  and  $\eta$ .

The GLL quadrature could be used to obtain an approximation to the integral in equation 2.26, taking the definition of the location of the internal points in the computational domain. Thus approximation of 2.26 could be expressed as,

$$\sum_{a,b} W_{a,b} \sum_{i,j} \widehat{\mathbf{V}}^*_{i,j} L_i(\xi_a) L_j(\eta_b) L_q(\xi_a) L_s(\eta_b) \mathbf{J}(\xi_a, \eta_b) . \quad (2.27)$$

$W_{a,b}$  represents the weighting coefficient for GLL quadrature,  $a$  and  $b$  represents the position of the node in the direction  $\xi$  and  $\eta$  respectively.

Even though equation 2.27 appears to be quite intimidating to deal with, the expression could be considerably simplified because of the fact that the system is discrete and the only the values at the nodal points are considered. Incorporating Lagrange polynomials allows the substitution

$$L_i(\xi_a) = \delta_{ia} = \begin{cases} 1 & i = a \\ 0 & i \neq a \end{cases} . \quad (2.28)$$

The Kronecker delta is expressed by  $\delta_{ia}$ . This substitution leads to a significant reduction of the non-zero elements in the simulation and leads to a much simpler expression. If the convection substep (example considered here) is considered, only a single term remains based on  $\mathbf{V}^*$  term in the convection substep equation which is,

$$W_{q,s} \mathbf{J}(\xi_q, \eta_s) \widehat{\mathbf{V}}^*_{q,s} . \quad (2.29)$$

All the governing terms could be simplified similarly and this process is repeated over all elements. A global matrix is assembled by collecting the contribution of each element and then this matrix system is solved to obtain solution for the unknown velocity and pressure fields at the nodal points.

Only the continuity of each function is required across the boundaries, with no condition imposed on the gradient (this condition is known as  $C_0$  continuity), even though the shape functions are higher-order polynomials within each element. It can be shown that the method achieves global exponential convergence (Karniadakis and Sherwin, 2005).

The numerical process used for this study has been demonstrated to give exponential spatial convergence as the number of internal nodes per element is increased (Thompson et al., 1996).

### Boundary conditions

The boundary conditions, regardless of the mesh were common for all the simulations performed. A no-slip condition was applied to the cross section wall. This condition implied that the velocity is zero at the surface of the cross section. For stationary simulations a Dirichlet boundary condition and for FSI cases a time-dependent Dirichlet boundary condition was employed for the velocity on the inlet and lateral boundaries. A Dirichlet boundary condition should have a specified value for the variables (Kreyszig, 2010) in this case velocity. The time-dependent Dirichlet condition has to be implemented for the FSI cases to account for the accelerated reference frame attached to the cross section. Thus, the inlet boundary was set to  $u = U$  and  $v = -\dot{y}$  for FSI cases and  $v = 0$  for stationary cases, where  $u, v$  are the velocities in the  $x$  and  $y$  directions, respectively.

At the outlet or at the boundary downstream of the body it was assigned that the  $\frac{\partial \mathbf{V}}{\partial \mathbf{n}} = 0$  where  $\mathbf{n}$  denotes the unit normal vector. This assumes that the flow does not spatially while exiting the domain. This is known as a Neumann boundary condition (where the gradient of a property is specified Tu et al. (2008)).

A Neumann condition for the pressure (where the gradient of a property is specified Tu et al. (2008)), where the normal gradient was calculated from the Navier–Stokes equations, was employed on the outlet, lateral and body surface (Gresho and Sani, 1987), while a Dirichlet condition for the pressure ( $p = 0$  was enforced at the outlet. The details of the method can be found in Thompson et al. (2006, 1996)

Although the physical validity of the outlet boundary condition is not quite true, this does not turn out to be a significant problem provided that the Reynolds numbers are low and the domain is sufficiently far away from the body.

### 2.4.3 Convergence and validation studies

#### Domain size

For all cases, a rectangular domain was employed where the inlet was placed  $20D$  from the centre of the body, while the outlet was situated  $60D$  away from the centre of the body. The lateral boundaries were placed  $20D$  away from the centre of the body. The macro element arrangement of the general domain is shown figure 2.1 while the element arrangement near

the cross sections are presented in figure 2.2.

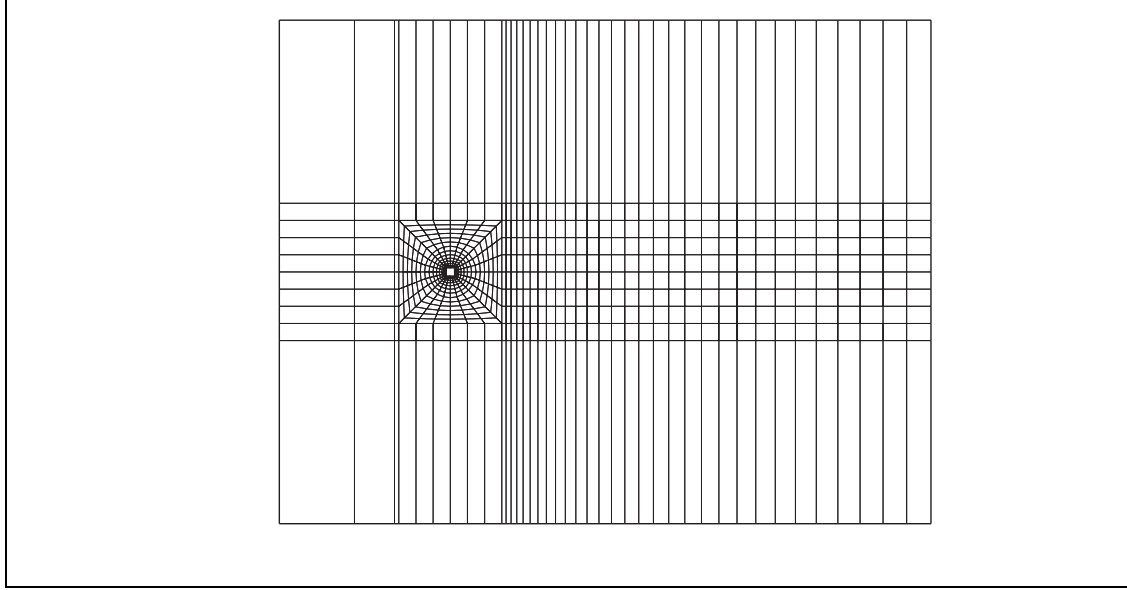


Figure 2.1: Macro element arrangement of the domain of the square cross section. The inlet extending  $20D$  towards upstream from the centre of the body, while the outlet extended  $60D$  downstream from the centre of the body. The lateral boundaries were placed  $20D$  away from the centre of the body

### Convergence

A series of simulations were carried out in order to ensure the results were grid independent. This was done by keeping the layout of the macro element the same and varying the order of the interpolation polynomial (*p-refinement*). The displacement amplitudes were compared against various polynomial orders. The time step was also altered to meet the Courant condition. The summary of the results are presented [The results table](#).

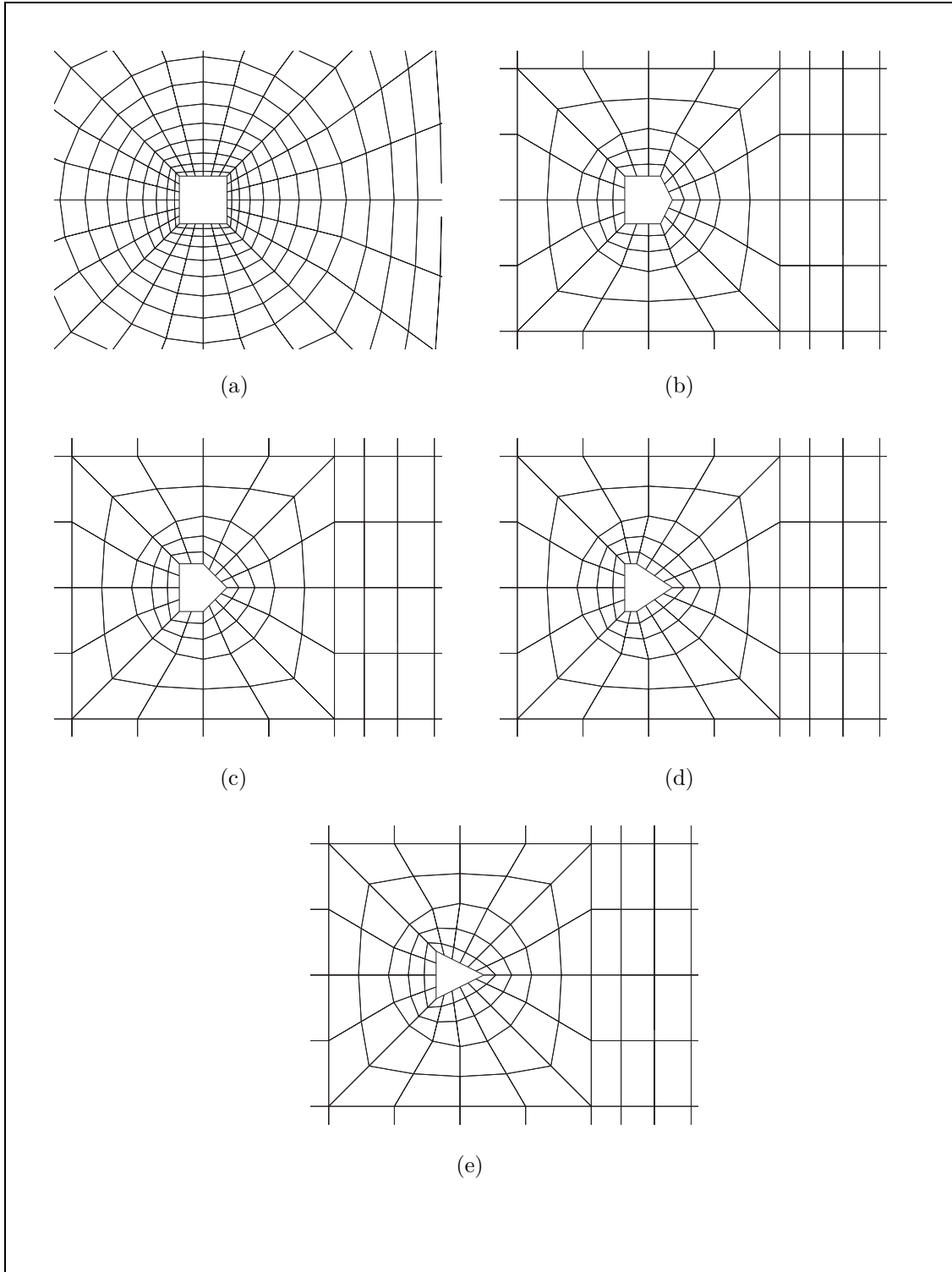


Figure 2.2: Configuration of the macro elements near the cross section. (a) square, (b)  $\frac{d}{l} = 0.75$ , (c)  $\frac{d}{l} = 0.5$ , (d)  $\frac{d}{l} = 0.25$  and (e) triangle.

## CHAPTER 3

---

# GOVERNING PARAMETERS OF FLUID-ELASTIC GALLOPING

### 3.1 Introduction

This chapter contains the formulation of non dimensional governing parameters namely, the combined mass-stiffness  $\Pi_1$  and the combined mass-damping  $\Pi_2$  and the results and discussion demonstrating the influence of them. These parameters are formulated by obtaining the relevant time-scales of the system followed by non-dimesnionlising the governing QSS oscillator equation.

First, the static body results are presented and discussed. Then, a comparison of Quasi-steady state data presented using the classical VIV parameters and the newly formulated  $\Pi_1$  and  $\Pi_2$  is presented and it is concluded that  $\Pi_2$  provides a better collapse for velocity amplitude and mean power compared the classical reduced velocity ( $U^*$ ) particularly because unlike  $U^*$ ,  $\Pi_2$  does not include a frequency component in it. This is followed by the presentation of QSS data and discussion on the influence of  $\Pi_1$  and  $\Pi_2$  on power, which concludes that the power transfer is a primary function of  $\Pi_2$  and a weak function of  $\Pi_1$ .

Following this, a comparison of the QSS data with Direct Numerical Simulations (DNS) is presented. This reveals that the power transfer of the DNS data is strongly influenced by both  $\Pi_1$  and  $\Pi_2$ . Further analysis reveals that there is a good agreement between QSS and DNS for velocity and power at substantially high  $\Pi_1$ . As  $\Pi_1$  decreases, the deviation

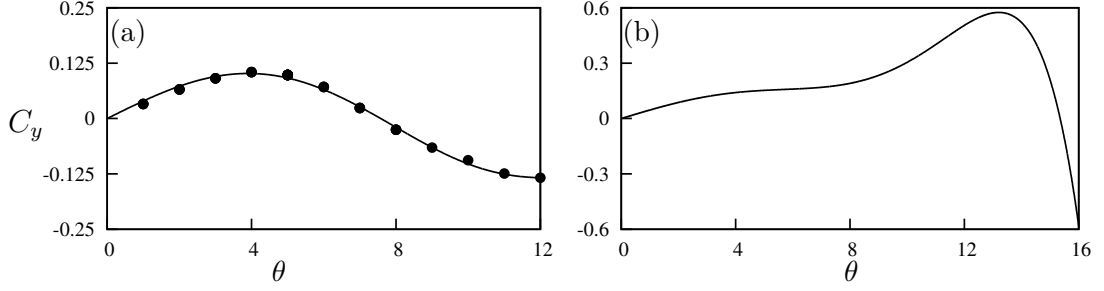


Figure 3.1: Lift coefficient,  $C_y$ , as a function of incidence angle  $\theta$ , for a static square cross section. (a) Data from simulations at  $Re = 200$  (b) data from Parkinson and Smith (1964) at  $Re = 22300$ . Points ( $\bullet$ ) are measurements from the simulations. At  $Re = 200$ . Curves in both plots are 7th-order interpolating polynomials used to predict the fluid forcing for the QSS model.  $C_y$  is the force coefficient of the force which occurs normal to the induced velocity.

(between QSS simulations and DNS) increases. Power spectral analysis of the DNS data shows a significant response at the vortex shedding at low  $\Pi_1$ . The relative strength was found out to be an inverse function of  $\Pi_1$ , which provides a clear explanation for the deviation between QSS simulations and DNS data at low  $\Pi_1$ . This is primarily due to the influence of vortex shedding where this effect is not accounted in the QSS model.

### 3.1.1 Static body results

Figure 3.1 shows the plots  $C_y$  as a function of  $\theta$ , as well as the interpolation polynomials. For high  $Re$  the polynomial incorporated by Parkinson and Smith (1964) was used. For low  $Re$  a 7<sup>th</sup> order polynomial was fitted using nonlinear least-squares regression. The coefficients of these polynomial fits are shown in table 3.1.

There are several differences that can be observed between high and low Reynolds number data. The peak value of  $C_y$  is significantly lower at  $Re = 200$  ( $C_y = 0.12$  at  $5^\circ$ ) compared to  $Re = 22300$  ( $C_y = 0.57$  at  $13^\circ$ ). The inflection point present around  $8^\circ$  for  $Re = 22300$  is not present at  $Re = 200$ . This agrees with the findings of Luo et al. (2003). It was concluded by Luo et al. (2003) that hysteresis in the system response occurs due to the inflection point in the  $C_y$  curve. Therefore hysteresis is not expected at  $Re = 200$ .

The range of incident flow angles where  $C_y$  remains positive is narrow at  $Re = 200$

Case	$a_1$	$a_3$	$a_5$	$a_7$
$Re = 200$	2.32	197.8	4301.7	30311.9
$Re = 22300$	2.69	168	1670	59900

Table 3.1: Coefficient values used in the 7th order interpolation polynomial for high ( $Re = 22300$ ) and low ( $Re = 200$ ) Reynolds numbers. These data are used as input data to calculate the right-hand side of Eq. 1.4 throughout this study.

( $0^\circ < \theta \leq 7^\circ$ ) compared to  $Re = 22300$  ( $0^\circ < \theta \leq 15^\circ$ ). This feature is what sustains galloping. Power is only transferred from the fluid to the supporting structure within this range of incident angles because fluid forces are acting in the direction of travel of, or in phase with, the oscillating body as demonstrated by equation ???. Incident angles beyond this range actually suppress the galloping and power is transferred in the opposite direction, i.e; from body to fluid. Therefore due to the overall smaller  $C_y$  and narrow range of angles where  $C_y$  is positive for  $Re = 200$  compared to  $Re = 22300$ , it is expected that the transferred power at  $Re = 200$  is significantly lower than at  $Re = 22300$ .

### 3.2 Formulation of the non-dimensionalised parameters $\Pi_1$ and $\Pi_2$

The natural time scales of the system could be obtained by linearising the quasi-steady equation of motion. (Eq: *\*\*KJ: equation of motion \*\**) and finding the eigenvalues. The non-linear terms of the forcing function are truncated and the equation of motion could be expressed as,

$$m\ddot{y} + c\dot{y} + ky = \frac{1}{2}\rho U^2 \mathcal{A}a_1 \left( \frac{\dot{y}}{U} \right), \quad (3.1)$$

After combining the  $\dot{y}$  terms and solving for eigenvalues the following solutions for the eigenvalues could be obtained.



$$\lambda_{1,2} = -\frac{1}{2} \frac{c - \frac{1}{2}\rho U \mathcal{A} a_1}{m} \pm \frac{1}{2} \sqrt{\left[ \frac{c - \frac{1}{2}\rho U \mathcal{A} a_1}{(m)} \right]^2 - 4 \frac{k}{m}}. \quad (3.2)$$

Galloping essentially occurs at low frequencies therefore it can be assumed that the spring is relevantly weak and therefore,  $k \rightarrow 0$ . Hence a single non-zero eigenvalue remains which is,

$$\lambda = -\frac{c - \frac{1}{2}\rho U \mathcal{A} a_1}{m}. \quad (3.3)$$

Further, if it is assumed that the mechanical damping is weaker than the fluid dynamic forces on the body the non zero eigenvalue could be further simplified to,

$$\lambda = \frac{\frac{1}{2}\rho U \mathcal{A} a_1}{m}. \quad (3.4)$$

In this representation  $\lambda$  represents the inverse time scale of the motion of the body due to the effect of long-time fluid dynamic forces (or forced due to the induced velocity). This term could also be re-written and  $\lambda$  could be expressed as

$$\lambda = \frac{a_1}{m^*} \frac{U}{D} \quad (3.5)$$

This form clearly shows the significant parameters that influences the inverse time scale of the system.  $\partial C_Y / \partial \alpha$ , the rate of change in the fluid dynamic force on the body, with respect to the induced angle of attack, is represented by  $a_1$ .  $\frac{U}{D}$  represents the inverse advective time scale of the incoming flow, and the mass ratio is resented by  $m^*$ . Increasing  $a_1$  would result in a rapid change of the fluid dynamic force with a small change of the induced angle  $\theta$ , which is proportional to transverse velocity  $\dot{y}$ . It can be seen in equation 3.5 that an increase of  $a_1$  would result in an increase of the inverse time scale or decrease the response time of the body. In contrast the mass ratio has the opposite effect where an increase in  $m^*$  will lead to a decrease in  $\lambda$ , since a heavier body (or a body with higher inertia) would have a slower response.

In order to find the relevant dimensionless groups of the problem, the time scale formulated could be used to non-dimensionalise the equation of motion. The equation of motion presented in Equation *\*\*KJ: put final equation of motion \*\** can be non-dimensionalised

### 3. GOVERNING PARAMETERS OF FLUID-ELASTIC GALLOPING

---

using the non dimensional time  $\tau$ , defined as  $\tau = t(a_1/m^*)(U/D)$ . The non-dimensional equation of motion could then be represented as,

$$\ddot{Y} + \frac{m^{*2}}{a_1^2} \frac{kD^2}{mU^2} Y = \left( \frac{1}{2} - \frac{m^*}{a_1} \frac{cD}{mU} \right) \dot{Y} - \frac{a_1 A_3}{m^{*2}} \dot{Y}^3 + \frac{a_1^3 a_5}{m^{*4}} \dot{Y}^5 - \frac{a_1^5 a_7}{m^{*6}} \dot{Y}^7. \quad (3.6)$$

The equation could be further altered by regrouping the coefficients into non-dimensional groups and could be expressed as,

$$\ddot{Y} + \frac{4\pi^2 m^{*2}}{U^{*2} a_1^2} Y = \left( \frac{1}{2} - \frac{c^* m^*}{a_1} \right) \dot{Y} - \frac{a_1 A_3}{m^{*2}} \dot{Y}^3 + \frac{a_1^3 a_5}{m^{*4}} \dot{Y}^5 - \frac{a_1^5 a_7}{m^{*6}} \dot{Y}^7, \quad (3.7)$$

$U^*$  is the reduced velocity which is the typical independent variable used in vortex-induced vibration studies.  $c^*$  is the non-dimensional damping parameter which is expressed as  $c^* = cD/mU$ .

By analysing equation 3.7 it is clear that five dimensionless parameters play a role in setting the response of the system. These are namely the stiffness, damping, mass ratio, the geometry and the Reynolds number. The stiffness is represented by the reduced velocity  $U^*$ , the damping by  $c^*$  and the mass ratio by  $m^*$ . The geometry and the Reynolds number are represented by the coefficients  $a_n$ , of the polynomial fit to the  $C_y$  curve. Using the natural time scales of the system, grouping of these non-dimensional parameters into two groups in the non-dimensional equation of motion, suggests that there are two groups that govern the response which are:  $\Gamma_1 = 4\pi^2 m^{*2}/U^{*2} a_1^2$  and  $\Gamma_2 = c^* m^*/a_1$ .  $\Gamma_1$  could be described as a combined mass-stiffness, where  $\Gamma_2$  could be expressed as a combined mass-damping parameter for a given geometry and a Reynolds number. It is assumed that the stiffness plays a minor role,  $\Gamma_2$  seems more likely parameter to collapse the data. The wind tunnel data in the classic paper of galloping by (Parkinson and Smith, 1964) adopted a parameter similar to  $\Gamma_2$  to collapse the data.

All of the quantities that formulate  $\Gamma_1$  and  $\Gamma_2$  except  $a_1$  in theory, could be obtained before an experiment. However in order to obtain the value of  $a_1$  static body experiments are required making it relatively difficult to obtain. Here, the  $Re$  and the geometry remains constant and therefore multiplying  $\Gamma_1$  with  $a_1^2$  and  $\Gamma_2$  with  $a_1$  suitable parameters could be obtained, and formulate a mass-stiffness parameter  $\Pi_1 = 4\pi^2 m^{*2}/U^{*2}$ , and a mass-damping parameter defined as  $\Pi_2 = c^* m^*$ . Therefore equation 3.7 can be written in terms of  $\Pi_1$  and  $\Pi_2$ .

$$\ddot{Y} + \Pi_1 \dot{Y} = \Pi_2 \dot{Y} - \frac{a_1 a_3}{m^{*2}} \dot{Y}^3 + \frac{a_1^3 a_5}{m^{*4}} \dot{Y}^5 - \frac{a_1^5 a_7}{m^{*6}} \dot{Y}^7, \quad (3.8)$$

From equation 3.8, it is clear that the governing parameters of the non dimensionlised equation are  $\Pi_1$   $\Pi_2$  and  $m^*$ . However, form closer inspection it is possible to see that  $m^*$  has an impact on the non-linear terms of the forcing function. The velocity pf the and hence the induced angle of attack needs to be very high in order for the non-linear terms to be applicable.

### 3.3 Quasi-steady state results

#### 3.3.1 Classical VIV parameters vs. $\Pi_1$ and $\Pi_2$ .

Vortex-induced vibrations being another form fluid-structure interaction which occurs in a slender structure, has been investigated as candidate for power extraction from external flows. Significant progress on this problem have been made by Bernitsas et al. (2008, 2009); Raghavan and Bernitsas (2011); Lee and Bernitsas (2011) and other colleagues in VIVCACE group in the University of Michigan. Hence, it may seem that it is reasonable to present the data in a fluid-elastic problem using the same parameters in a VIV problem.

QSS data presented in figure 3.2 at  $Re = 200$ , shows a comparison between classical VIV and the newly formulated parameters presented as independent variables. The displacement amplitude, velocity amplitude and the mean power is presented in sub-figures (a), (c) and (e), as functions of the classical VIV parameter  $U^*$  for different  $\zeta$ . The same data as functions of  $\Pi_2$ , are presented in sub-figures (b), (d) and (f), for various, reasonably high values of  $\Pi_1$  *\*\*KJ: put the parameters used section\*\**. Sub-figure (e) shows a similar trend to Barrero-Gil et al. (2010). The Value of the peak power remains constant. However, the power curve shifts to the right as  $\zeta$  is increased. Here, in figure 3.2 the maximum dimensionless power is achieved at two times the velocity at which the galloping starts, which is similar to the observations made by Barrero-Gil et al. (2010); Vicente-Ludlam et al. (2014). An excellent collapse for velocity amplitude and mean power could be observed on the data, presented using the dimensionless group  $\Pi_2$ , formulated using the natural time scales of the system. This implies that essentially velocity amplitude and the mean power is dictated by  $\Pi_2$  which furthermore, implies that the natural frequency of the system which

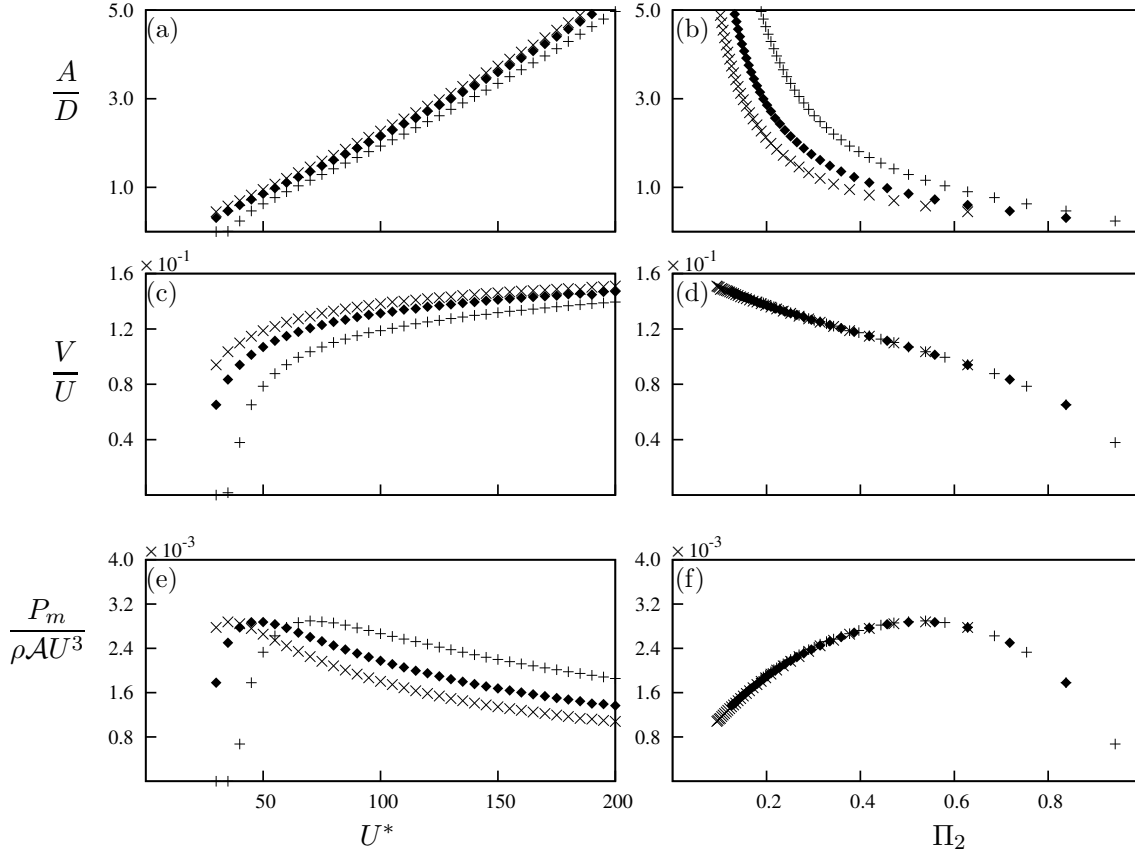


Figure 3.2: Displacement amplitude, velocity amplitude and dimensionless mean power data as functions of two different independent variables. Data presented in (a), (c) and (e) using the classical VIV parameter  $U^*$ , obtained at  $Re = 200$  and  $m^* = 20$  at three different damping ratios:  $\zeta = 0.075$  ( $\times$ ),  $\zeta = 0.1$  ( $\blacklozenge$ ) and  $\zeta = 0.15$  (+). (b) (d) and (f) are the same data presented using the combined mass-damping parameter ( $\Pi_2$ ) as the independent variable. Even though  $\Pi_1$  varies in the range of  $0.4 \leq \Pi_1 \leq 17.5$ , it is clear that the power is a function of  $\Pi_2$  only.

is used to scale  $U^*$ ,  $\zeta$  and  $\Pi_1$  does not have a significant influence on the behaviour of the system, unlike VIV, which is a resonant phenomenon.

### 3.3.2 High and low $Re$ data

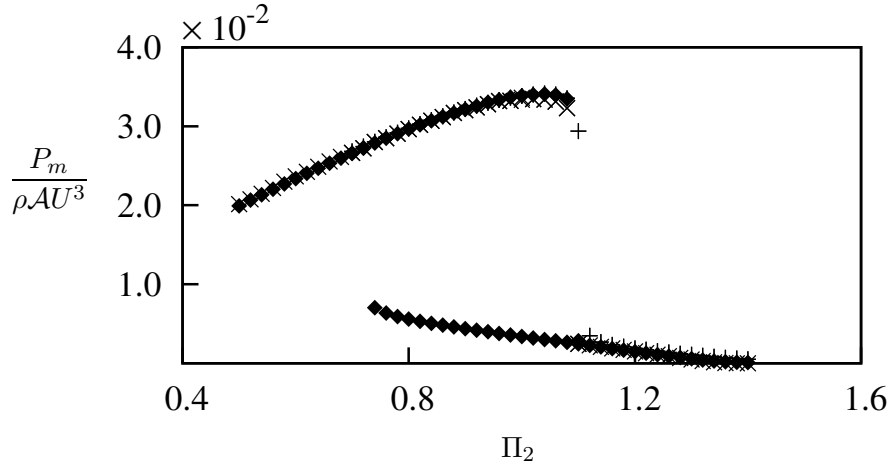


Figure 3.3: Dimensionless mean power as a function of  $\Pi_2$ . Data presented at (a)  $Re = 22300$ ,  $\Pi_1 = 200$  ( $\times$ ),  $\Pi_1 = 2000$  ( $\blacklozenge$ ) and  $\Pi_1 = 10000$  ( $+$ ). Hysteresis could be observed at high  $Re$ .

The successful collapse of data, mean power in particular using  $\Pi_2$  for low Reynolds number ( $Re = 200$ ), could be replicated at high Reynolds numbers. An example case is presented in figure 3.2 at  $Re = 22300$  for selected values of  $\Pi_1$ . The successful collapse of mean power data at high Reynolds numbers shows that suitability of using  $\Pi_2$  as an independent variable across a large range of Reynolds numbers.

Hysteresis is evident in the high Reynolds number case ( $Re = 22300$ ). Manipulating the initial condition (initial displacement) lead to obtaining different solutions for the same  $\Pi_2$  value. The upper and lower branch were obtained by giving an initial displacement which was higher than the expected amplitude and providing a lower initial displacement respectively. Even though in theory, there is a possibility of a third state, this unstable branch could not be achieved with a time integration method (also observed by (Vio et al., 2007)) such as the one employed in this study.

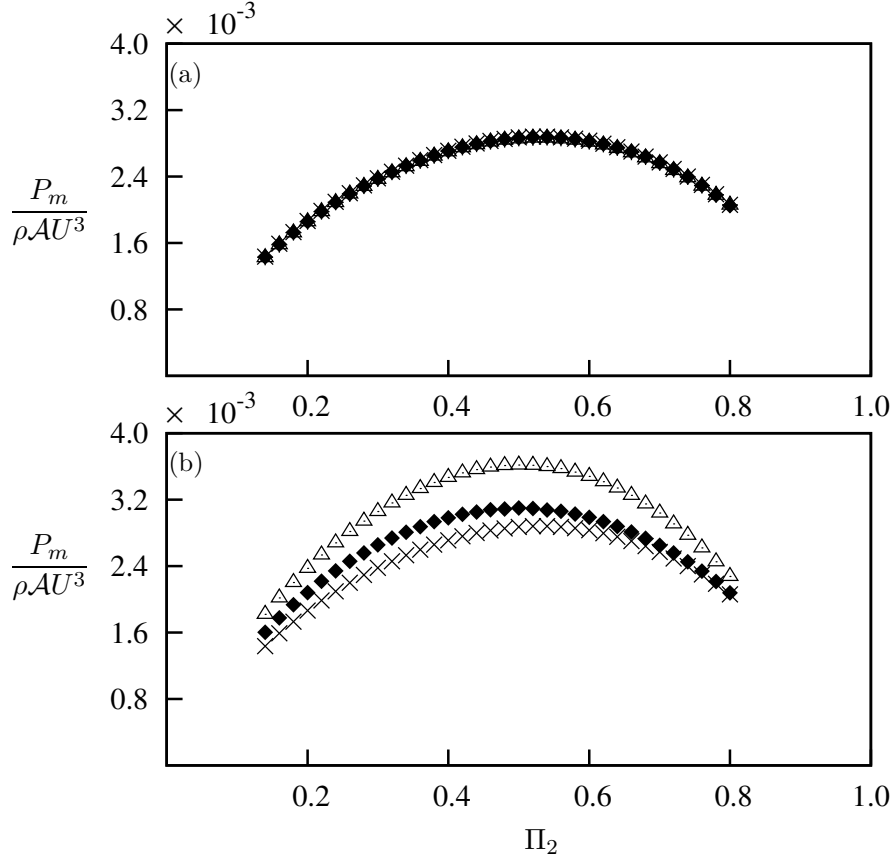


Figure 3.4: Dimensionless mean power as a function of  $\Pi_2$  obtained using the QSS model at  $Re = 200$ . (a) High  $\Pi_1$ ; data presented at four different combined mass-stiffness levels.  $\Pi_1 = 10$  ( $m^* = 20$ ,  $U^* = 40$ ) ( $\times$ ),  $\Pi_1 = 100$  ( $m^* = 80$ ,  $U^* = 50$ ) ( $+$ ),  $\Pi_1 = 500$  ( $m^* = 220$ ,  $U^* = 60$ ) ( $\blacklozenge$ ) and  $\Pi_1 = 1000$  ( $m^* = 400$ ,  $U^* = 40$ ) ( $\triangle$ ). (b) Low  $\Pi_1$ ; data presented at  $\Pi_1 = 10$  ( $\times$ ),  $\Pi_1 = 0.1$  ( $\blacklozenge$ ), and  $\Pi_1 = 0.01$  ( $\triangle$ ).

### 3.3.3 Dependence on mass-stiffness, $\Pi_1$

From the results of sections 3.3.1 and 3.3.2 shows essentially a single variable governs the mean extracted power, which is the combined mass-damping parameter,  $\Pi_2$ . The time scale analysis carried out in section 3.2 shows that not only  $\Pi_2$  but also  $\Pi_1$  influences the system. Previous studies such as Bouclin (1977) have also reported a complex interaction between the displacement amplitude and the natural frequency, for high natural frequencies in particular; or in this instance equivalent to low values of  $\Pi_1$ . This section investigates the impact of  $\Pi_1$  further. The overall behavior of the system is divided into two regimes, one for “high”  $\Pi_1$  and the other for “low”  $\Pi_1$  and analysed.

The mean power as a function of  $\Pi_2$  for a range of values of  $\Pi_1$  is presented in figure 3.4. In the two subfigures presented, (a) shows the data for  $\Pi_1 \geq 10$ , while (b) shows data for  $\Pi_1 \leq 10$ . The excellent collapse in figure 3.4(a) shows that for  $\Pi_1 \geq 10$ , the mean power is independent of  $\Pi_1$ .

In contrast figure 3.4(b) shows that for low values of  $\Pi_1 \leq 10$ , the predicted mean power increases as  $\Pi_2$  decreases. This indicates that at this region ( $\Pi_1 < 10$ ), the mean power is a weak function of  $\Pi_1$ ; hence, providing a distinction between high and low regimes of  $\Pi_1$ . The mean extracted power is only a function of  $\Pi_2$  where  $\Pi_1 \geq 10$  or for high  $\Pi_1$ . For low values,  $\Pi_1 < 10$ , the mean power becomes a strong function of  $\Pi_2$  and a weak function of  $\Pi_1$ .

It is clear that regardless of the value of  $\Pi_1$ , the variation of power with  $\Pi_2$  is essentially the same. As  $\Pi_2$  is increased, the mean extracted power will increase to the point which, it will attain some maximum value and then decrease. This relationship between power and  $\Pi_2$  could be explained by analysing the time histories of selected cases. AS an example, data at  $\Pi_1 = 10$ ,  $m^* = 20$  and  $Re = 200$  are presented in figure 3.5. Three major regions where the value of the power curve are considered. These regions are  $\Pi_2$  less than (region 1), equal to (region 2) and greater than (region 3) to the  $\Pi_2$  value where the mean power is at its maximum.

The damping is low in region 1 ( $\Pi_2 = 0.15$ ) in comparison with region 2 and 3. Although this may lead to larger oscillations, according to equation 2.1 damping is required to dissipate and therefore extract power. Hence, a low mean power output is gained at low damping. The high velocity amplitude leads the equivalent incident angle  $\theta$  to exceed

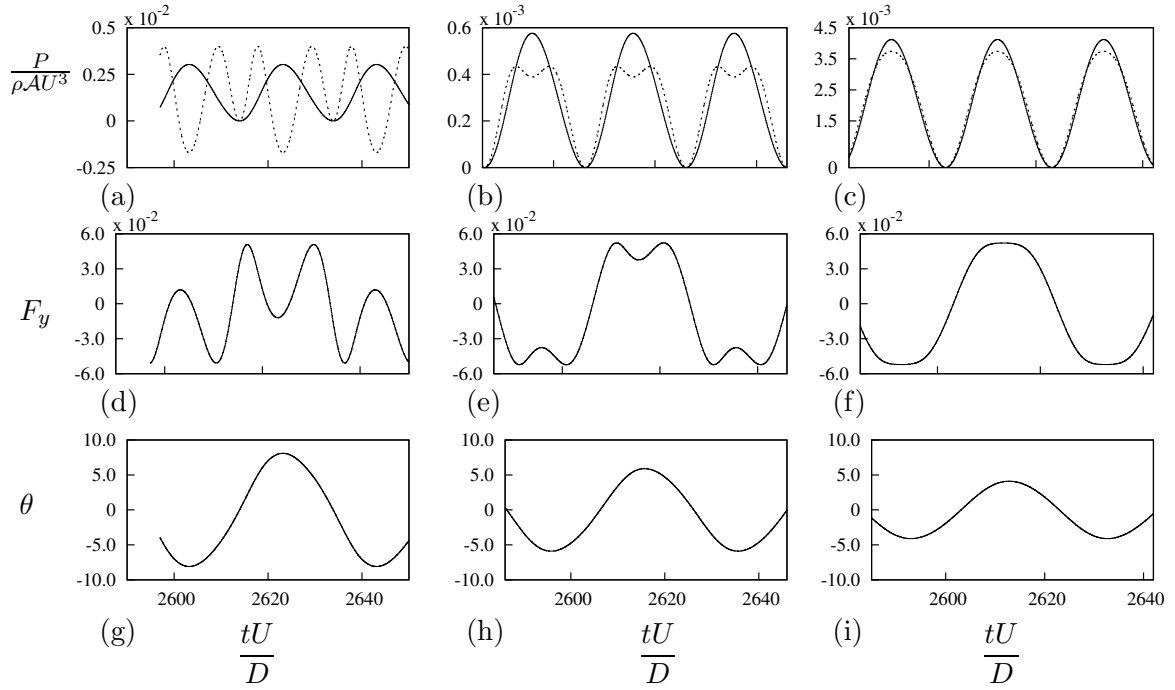


Figure 3.5: Time histories of  $P_t$ ,  $P_d$ ,  $F_y$  and  $\theta$  at  $\Pi_2 = 0.15, 0.54$  and  $0.8$  from the QSS model. Data was obtained at  $m^* = 20$ ,  $\Pi_1 = 10$  and  $Re=200$ . The time histories of  $P_t$  (—) and  $P_d$  (---) are presented for: (a)  $\Pi_2 = 0.15$ ; (b)  $\Pi_2 = 0.54$ ; (c)  $\Pi_2 = 0.8$ . Time histories of the instantaneous force  $F_y$  for: (d)  $\Pi_2 = 0.15$ ; (e)  $\Pi_2 = 0.54$ ; (f)  $\Pi_2 = 0.8$ . Time histories of the instantaneous angle  $\theta$  for: (g)  $\Pi_2 = 0.15$ ; (h)  $\Pi_2 = 0.55$ ; (i)  $\Pi_2 = 0.8$ .



the positive range of  $C_y$  (i.e.  $0 < \theta < 6^\circ$  as shown in figure 1.3(a)) resulting a negative dissipated power by damping  $P_d$  over some portion of the cycle as shown in figure 3.5 (a). The galloping force  $F_y$  and the transverse velocity  $\dot{y}$  are not in phase in this portion of the cycle where the force opposes the direction of travel. As a consequence, during this period of time the opposite of what is expected happens, where the power is transferred from the structure to the fluid. Since  $\Pi_2$  is substantially low, from an energy perspective, the mechanical damping is not sufficient to remove the energy transferred from the fluid to the structure through work during other times of the cycle. Hence, as depicted by the negative region of  $P_d$ , this excess energy is transferred back to the fluid.

A clear sinusoidal signal of both  $P_d$  and  $P_t$  (3.5(c)) could be observed at region 3 where  $\Pi_2 = 0.8$  and the damping constant is high. The equivalent incident angle  $\theta$  (which for small values, is proportional to the transverse velocity of the body) is in phase with the galloping force  $F_y$  as shown in figures 3.5(f) and 3.5(i). The velocity amplitude is small in this case resulting  $\theta$  falling within the range where the fluid-dynamic force ( $F_y$ ) increases within the incident angle (i.e.  $0 < \theta \leq 5^\circ$  as shown in figure 3.1(a)). These conditions are favourable for high power output according to equation ???. Be that as it may, in this case the velocity is limited because of the high damping resulting relatively low fluid dynamic forcing.

A harmony between the high and low values of damping could be found at region 2 ( $\Pi_2 = 0.54$ ). It is evident that  $P_d$  remains periodic but is not a pure sinusoidal signal. Two ‘peaks’ are present in a single half cycle from the time history graph of  $P_d$  as shown in figure 3.5(b). The velocity amplitude actually exceeds the equivalent incident angle where the fluid-dynamic forces peaks (i.e.  $\theta = 5^\circ$  in 1.3 (a)) in this scenario. The dip in between the two peaks in a single half cycle correspond approximately to the time where the transverse velocity is higher than 0.09 and  $F_y$  is decreasing with increasing transverse velocity. As this region is the best compromise between region 1 and region 3, the maximum mean power could be attained in this region. Region 2 could also be identified as the “sweet spot” for energy extraction as the damping is high enough to obtain a high power output while not so high for the motion to be completely suppressed.

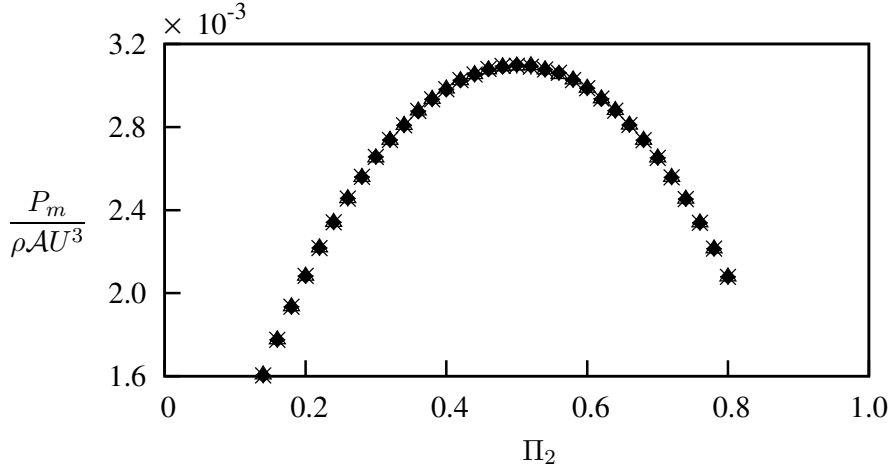


Figure 3.6: Dimensionless mean power as a function of  $\Pi_2$  obtained using QSS model at  $\Pi_1 = 0.1$ . Data presented at  $m^* = 2$  ( $\blacklozenge$ ),  $m^* = 20$  ( $\triangle$ ) and  $m^* = 50$  ( $*$ ). The mass ratio does not have an effect on  $\Pi_1$  even at low  $\Pi_1$ .

#### 3.3.4 Dependence on the mass ratio $m^*$

It is clear that the mean extracted power is only a function of  $\Pi_2$  for high values of  $\Pi_1$ . However, the question remains about the region of low  $\Pi_1$ . Does the variation of the mean extracted power occur purely as a function of  $\Pi_1$ , or does the mass ratio also has an influence on power? The QSS model was solved by varying the values for  $m^*$  but keeping the  $\Pi_1$  fixed. In other words  $\Pi_1$  was changed by changing the stiffness of the system.

It is clear from figure 3.6, data presented being the mean extracted power as a function of  $\Pi_2$ , for a fixed  $\Pi_1 = 0.1$ , for three different values of  $m^*$ , that mean power is independent of  $m^*$ , hence, it is only a function of  $\Pi_1$  and  $\Pi_2$ .

#### 3.3.5 Comparison with DNS data

The main drawback of the QSS model is that the instantaneous lift generated by the induced velocity is the only driving force of the system. However, in realistic scenarios the flow is far more complex and the only force affecting the system is not the induced lift. Force generated due to vortex shedding is one of the prominent forces in these systems. Hence, when the QSS model is being used, one of the essential assumptions is that the effect of vortex shedding is minimal. Due to this reason the model has been always used at high Reynolds numbers and at high  $m^*$ . Therefore, a study to identify the limiting parameters

of the QSS model at low Reynolds numbers was carried out using a comparison of QSS data with DNS results.

A sinusoidal forcing function was introduced to the QSS model in order to account for the forcing by vortex shedding by Joly et al. (2012). In this study displacement data obtained by the QSS model and the DNS simulations were compared which agreed well at low Reynolds numbers. The data were obtained at zero damping levels. As the primary focus of this study is the behaviour and the power transfer of the system, analysing the behaviour of the system with increasing damping is of interest.

Figure 3.7 provides a comparison between QSS and the DNS results. The maximum displacement, velocity and mean extracted power are presented as a function of  $\Pi_2$ . A range of values of  $\Pi_1$  are compared to the QSS model data for  $\Pi_1 = 10$ . Only little variation with  $\Pi_1$  could be found in the displacement amplitude (figure 3.7(a)) and velocity amplitude (3.7(b)). Thus the comparison between the QSS model and the DNS simulation is quite satisfactory for these two quantities. In contrast, there is a significant influence of both  $\Pi_1$  and  $\Pi_2$  on the mean extracted power which is presented in figure 3.7(c). This discrepancy become more vivid in the regions where the value of  $\Pi_1$  is low. These regions has the largest discrepancy between the QSS model and DNS data. A comparison of data between figures 3.7(c) and 3.4(a) shows that  $\Pi_1$  has a much more significant influence on the extracted power than the predictions by the QSS model for low  $\Pi_1$  values. Indeed as discussed in section 3.3.3 the QSS model predicts that the mean extracted power should increase with decreasing  $\Pi_1$  when  $\Pi_1$  moves to the low  $\Pi_1$  region (figure 3.4(b)). However, the DNS data show sort of an opposite result where the extracted mean power decreases with decreasing  $\Pi_1$ .

The dependence of the mean extracted power on  $\Pi_1$  is clearly shown in figure 3.8(a). Here, the maximum power extracted for a given value of  $\Pi_1$ , over all values of  $\Pi_2$  (essentially the value of extracted power at the turning point), is plotted as a function of  $\Pi_1$ . A quadratic fit was used obtain these values presented in figure 3.6 and finding the mean extracted power at the turning point of the power curve. It is clear that there is a rapid decrease in extracted power as  $\Pi_1 \rightarrow 0$ .

Figure 3.8(a) also shows that  $\Pi_1$  is important to higher values than predicted by the QSS model. The maximum extracted power is essentially independent of  $\Pi_1$  for  $\Pi_1 > 10$ ,

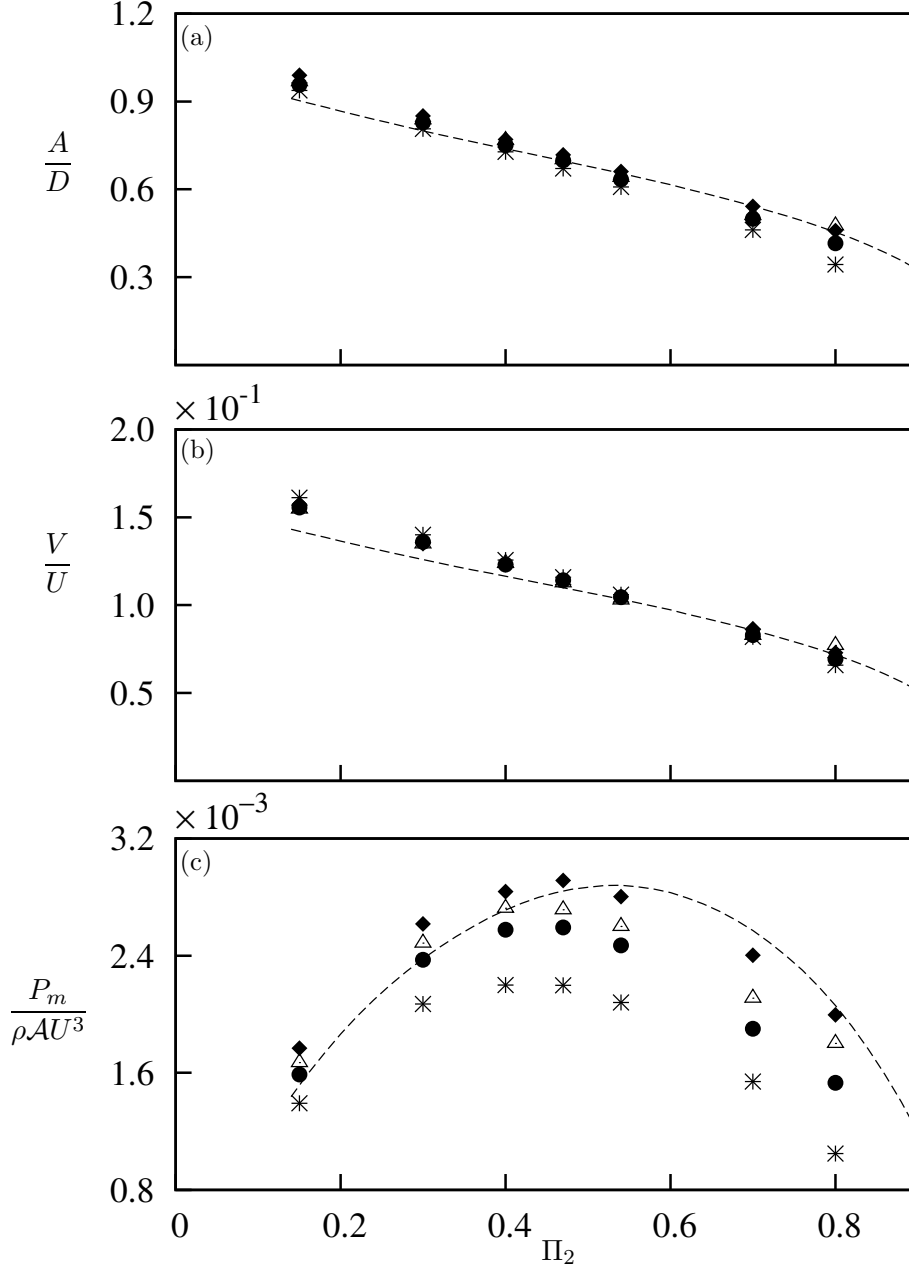


Figure 3.7: Comparison of data generated using the quasi-static model and full DNS simulations at (a) Displacement amplitude, (b) velocity amplitude and (c) dimensionless mean power as functions of  $\Pi_2$ . Data were obtained at  $Re = 200$  at four values  $\Pi_1 = 10$  ( $m^* = 20.13$ ) (\*),  $\Pi_1 = 60$  ( $m^* = 49.31$ ) (●),  $\Pi_1 = 250$  ( $m^* = 100.7$ ) (△) and  $\Pi_1 = 1000$  ( $m^* = 201.3$ ) (◆). The QSS data at  $\Pi_1 = 10$  (---).

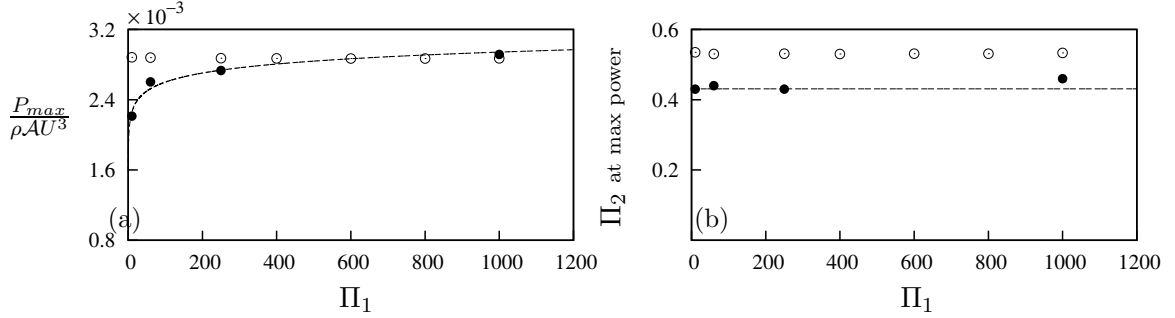


Figure 3.8: (a) Maximum power and (b) the value of  $\Pi_2$  at maximum power of QSS data (○) and DNS data (●), as functions of  $\Pi_1$ . For the DNS data, The maximum power asymptotes to an upper value with increasing  $\Pi_1$ , while the value of  $\Pi_2$  where maximum power occurs is relatively insensitive to  $\Pi_1$ . The maximum power of the QSS data remains relatively constant, as does the value of  $\Pi_2$  where maximum power occurs. The dash curve (---) of (a) follows the logarithmic fit of the maximum power which is  $P_{max}/\rho AU^3 = 1.48 \times 10^{-4} \ln(\Pi_1) + 1.9 \times 10^{-3}$ . The dashed curve in (b) shows the value  $\Pi_2 \simeq 0.43$ .

which could be observed by the open symbols in the figure. Nonetheless a significant dependence on  $\Pi_1$   $\Pi_1 < 250$  could be observed in the extracted power. Yet, as the  $\Pi_1$  increases the mean power converges to that of the values predicted by the QSS model.

The value of  $\Pi_2$  at the turning point of the power curve or the point of maximum power is shown in figure 3.8(b). The open symbols represents the values predicted by the QSS model while the values predicted by DNS simulations are represented by the close symbols. These two values does not coincide where the DNS predictions (shown with a dashed line) has a value around 0.41 while the predictions of the QSS model has a value of 0.5. Regardless, both QSS model and DNS show that while the mean power is a reasonably strong function of  $\Pi_1$ , the value of  $\Pi_2$  at the point of maximum power output is relatively unaffected.

The percentage discrepancy between the QSS DNS extracted power data as a function of  $\Pi_1$  was calculated using equation 3.9 in order to further quantify the performance of the QSS model.

$$\% \text{ error} = \left| \frac{P_{m(QSS)} - P_{m(DNS)}}{P_{m(DNS)}} \right| \times 100. \quad (3.9)$$

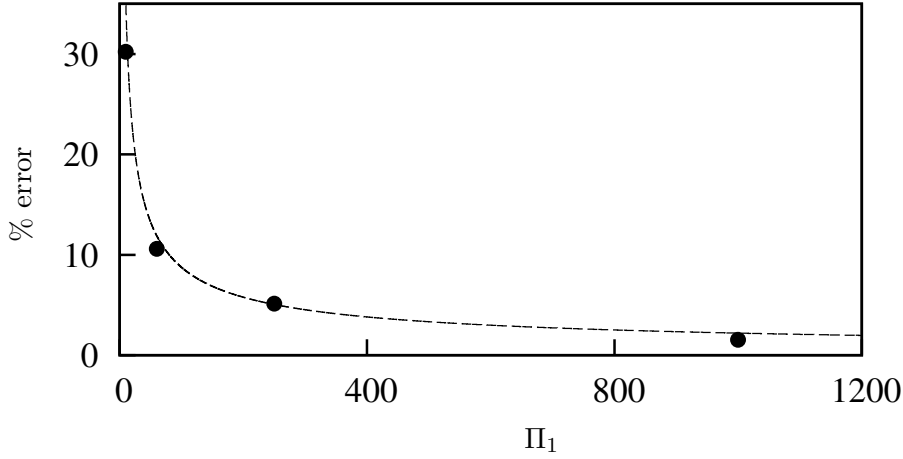


Figure 3.9: The percentage error between the maximum power obtained using DNS data and predicted by QSS model as a function of  $\Pi_1$ . The QSS model prediction is worst for low values of  $\Pi_1$ . The dash curve (---) follows the power law fit of the percentage error which is  $\%error = 138.697\Pi_1^{-0.6}$ .

Figure 3.9 shows the data obtained by this error calculation along with a power-law best fit  $138.697\Pi_1^{-0.6}$ . It clearly shows that as  $\Pi_1$  increases the percentage error between QSS model and DNS quickly decreases. But, the discrepancy between the two can be quite large, about 30% at low values of  $\Pi_1$ .

The influence of vortex shedding could be one of the likely reasons for this discrepancy at low  $\Pi_1$  which is not accounted for in the QSS model. The frequency spectra of the velocity of the body from DNS cases at varying  $\Pi_1$  at a value of  $\Pi_2 = 0.47$  which is close to the value at which the mean extracted power is a maximum, were plotted to test this hypothesis. Figure 3.10 shows this power spectrum plots along with the original time histories of the transverse velocities of the body.

This figure shows the velocity signals at  $\Pi_1 = 0.8$  and  $\Pi_2 = 10, 60, 250$  and  $1000$  and the corresponding spectrum. A significant component around  $fd/U = 0.156$  which can be identified as the vortex shedding frequency could be seen in the spectral data. As  $\Pi_1$  increases a clear reduction of the magnitude of the component at the vortex shedding frequency could be observed. This indicates that the influence of vortex shedding is much more prominent at low  $\Pi_1$ , therefore resulting in larger deviations from quasi-steady state results. This builds on the work of Joly et al. (2012), which was conducted at zero damping,

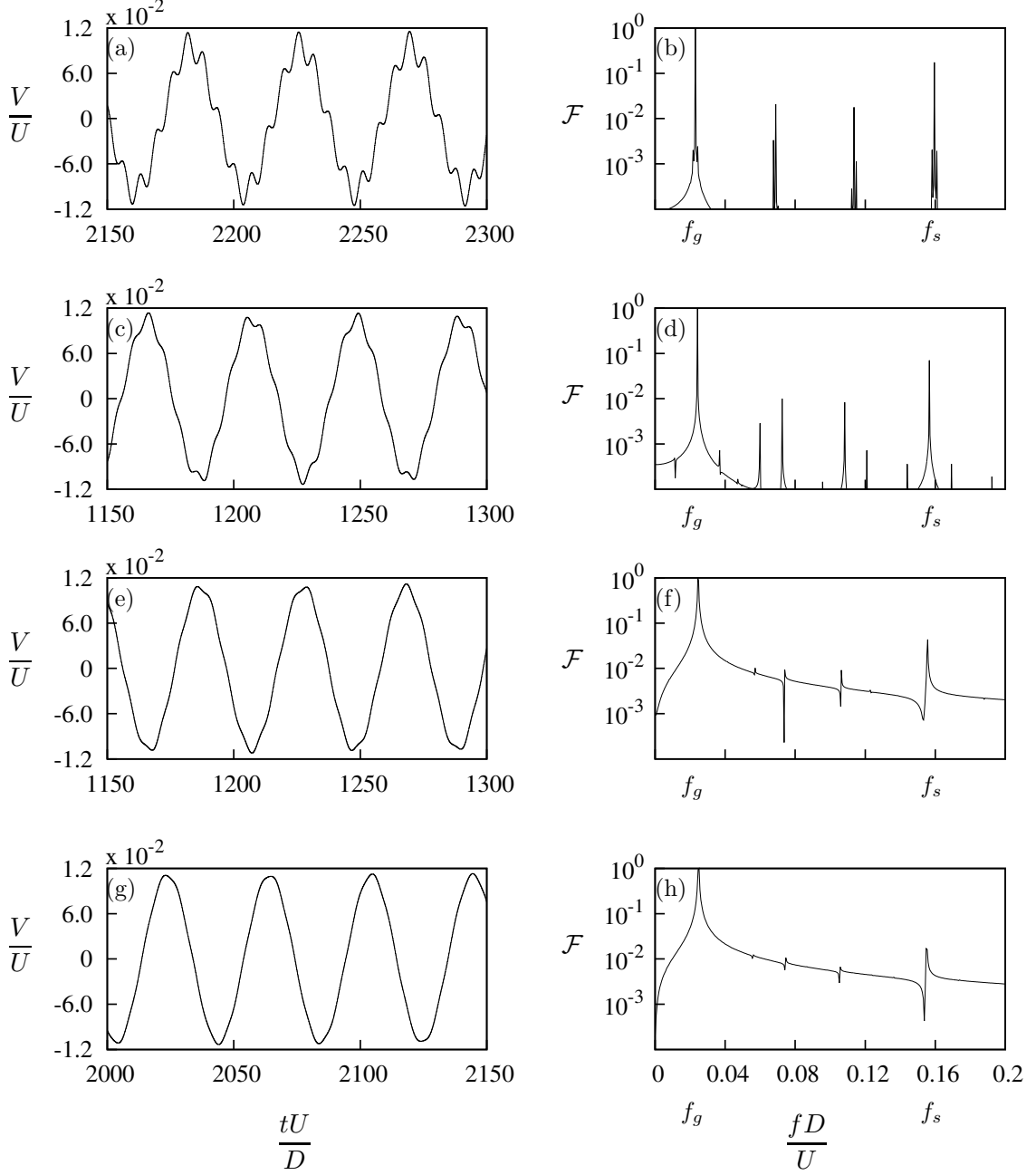


Figure 3.10: Velocity signal (right) and the corresponding power spectrum (left) of the DNS data at four values of  $\Pi_1$  at  $\Pi_2 = 0.47$ . (a) and (b)  $\Pi_1 = 10$ , (c) and (d)  $\Pi_1 = 60$ , (e) and (f)  $\Pi_1 = 250$ , (g) and (h)  $\Pi_1 = 1000$ .  $U^*$  is kept at 40 therefore the mass ratio increases as  $\Pi_1$  increases. It is evident that the influence of vortex shedding reduces as the inertia of the system increases.

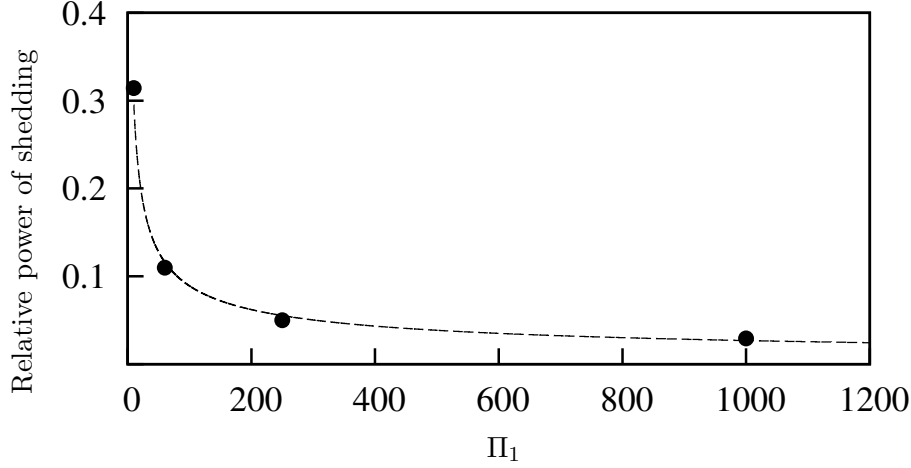


Figure 3.11: The relative power of the vortex shedding as a function of  $\Pi_1$ . The relative power of the vortex shedding decreases as  $\Pi_1$  increases. The dash curve (---) follows the power law fit of the percentage error which is  $\text{Relative power} = 0.977\Pi_1^{-0.52}$ .

that implied that mean extracted power would be influenced by vortex shedding at low mass.

This influence is explicitly shown here. Figure 3.11 plots the relative intensity of the component at the vortex shedding frequency to the component at the galloping or oscillation frequency in the spectra of figure 3.10.

The relative strength of the vortex shedding is seen to be large at low values of  $\Pi_1$  and drastically decreases as  $\Pi_1$  is increases. This follows a similar behaviour to the discrepancy between the QSS and DNS mean extracted power shown in figure 3.9. From the figure to could be seen that the variation of the relative power of the vortex shedding frequency to the galloping frequency is similar to  $0.977\Pi_1^{-0.52}$

The difference between the power predicted by the QSS and DNS models scales with  $\Pi_1^{-0.6}$  while the relative power at the vortex shedding frequency scales with  $\Pi_1^{-0.52}$ . Both these scalings are quite similar which is closer to  $1/\sqrt{\Pi_1}$ . Though it is unequivocal, this correlation is a strong indication that the discrepancy between QSS and DNS is result of the influence of vortex shedding, even though the frequencies of vortex shedding and galloping remains well separated by around similar amount for all values of  $\Pi_1$  (Figure 3.11). The data presented in figure 3.11 also give some sort of an indication of the strength of any vortex shedding correction term that might be added to the QSS model in an effort to decrease



the discrepancy between it and the DNS simulations.

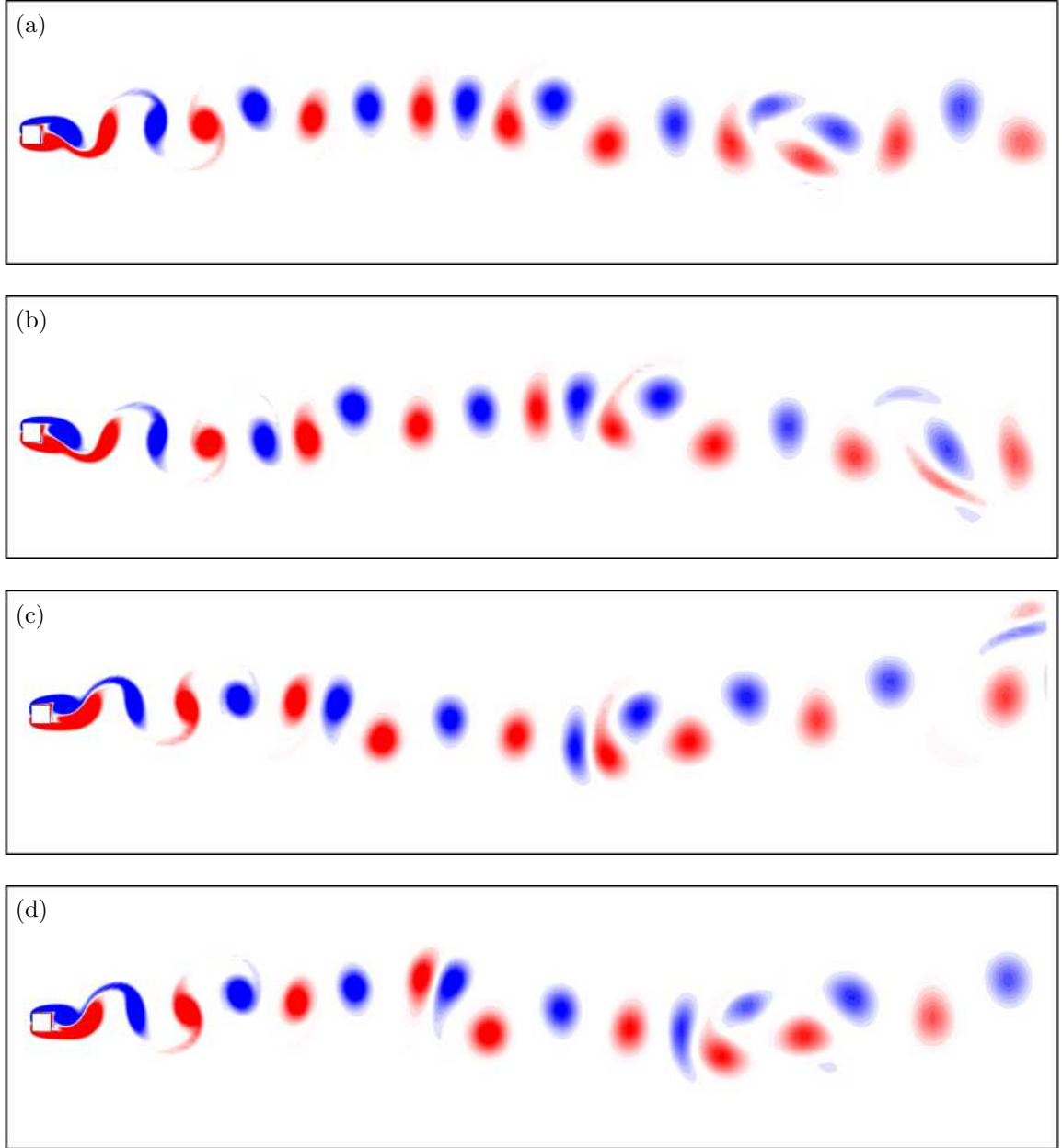


Figure 3.12: Vorticity plots of the flow at arbitrary instants at  $\Pi_2 = 0.47$ . (a)  $\Pi_1 = 10$ , (b)  $\Pi_1 = 60$  (c)  $\Pi_1 = 250$  and (d)  $\Pi_1 = 1000$  at  $Re = 200$ . Contours show vorticity at levels between  $\pm 1$ .

More information can be gained by analysing the flow field. Figure 3.12 shows the flow field data at arbitrary instances where the values of  $\Pi_2$  are close to the point of

---

the maximum power at different  $\Pi_1$  a clear wavelength could be observed in this figure. Qualitatively, this can be interpreted as such that at high  $\Pi_1$ , the vortex shedding is simply superimposed over the path of motion of the cylinder. A decrease in amplitude of this wave could be observed at low  $\Pi_1$  which may be caused due to the higher levels of non-linear interactions between vortex shedding and galloping. Such an argument is constant with the data of figure 3.11 that show the increasing significance of vortex shedding as  $\Pi_1$  decreases. Bundled together, this also to a certain extent helps to explain the discrepancy between the mean extracted predicted by the QSS and DNS models at low  $\Pi_1$ , highlighted in figure 3.9.

## 3.4 Summary of the governing parameters of fluid-elastic galloping

An analysis of the power transfer of a square body under fluid-elastic galloping is presented in this chapter. This analysis was carried out by solving the quasi-steady state oscillator model equation with the use of numerical integration. Dimensionless groups were formulated by through the relevant time scales by linearising the QSS equation. In comparison with classical VIV parameters i.e.  $\zeta$  and  $U^*$  a good collapse could be obtained with these newly formulated parameters. Having the collapsed data using the dimensionless groups further strengthens the argument that the velocity amplitude and the power transfer of the system does not depend on the natural frequency of the system over a large range of natural frequencies.

Although  $m^*$  is shown to be an independent parameter in equation 3.8, the results show that the system is only a function of  $\Pi_1$  and  $\Pi_2$  essentially. This could be explained by inspecting equation 3.8, which shows that  $m^*$  only has an impact on the forcing terms which are non-linear in relation to the velocity of the body. In order for these terms to be appreciable, the velocity of the body, and hence, the induced angle of attack need to be quite high, which for the range of parameters tested here, appears not to be the case.

Comparing with direct numerical simulation data, the quasi steady state model provide a good approximations of the power output when the  $\Pi_1$  of the system is relatively large. But, at low values of  $\Pi_1$ , the prediction has a large discrepancy, as the QSS model does

not account for the impact of vortex shedding, where the influence increase as the  $\Pi_1$  is decreased. That being said, the QSS model does provide quite a reasonable prediction of the value of  $\Pi_1$  at the point where the maximum power is produced. Both the error in predicted maximum power between the QSS and the DNS models, and the relative power of the vortex shedding, have been quantified. It scale similarly to  $1/\sqrt{\Pi_1}$ .

The presence of a clear wave length in the flow field at high  $\Pi_1$  and the reduction of this wavelength as  $\Pi_1$  decreases provides more evidence to the fact that vortex shedding has a complex influence on galloping systems.

## CHAPTER 4

---

# FREQUENCY RESPONSE OF THE SYSTEM

### 4.1 Introduction

### 4.2 Linear frequency of the system

The eigenvalues of the linearised QSS model could be found in equation 3.2. The term under the square root (equation 4.1) of this equation can be used to express the frequency of the system provided that the term is complex. Hence, the frequency could be defined as the imaginary portion of this complex number

$$f = \sqrt{\left[ \frac{c - \frac{1}{2}\rho U A a_1}{(m)} \right]^2 - 4 \frac{k}{(m)}}. \quad (4.1)$$

By substituting  $c^*$ ,  $m^*$  and  $U^*$  equation 4.1 could be non-dimensionalised as follows:

$$f = \sqrt{\left[ c^* \left( \frac{U}{D} \right) - \frac{1}{2} \frac{a_1}{m^*} \left( \frac{U}{D} \right) \right]^2 - 4 \left( \frac{U}{D} \right)^2 \frac{2\pi}{U^*}}. \quad (4.2)$$

This can then be rewritten as

$$f = \sqrt{\left( \frac{U}{D} \right)^2 \left( c^* - \frac{a_1}{2m^*} \right)^2 - 4 \left( \frac{U}{D} \right)^2 \left( \frac{2\pi}{U^*} \right)^2}. \quad (4.3)$$

#### 4.3. FINDING THE TERMINAL VELOCITY OF THE BODY WHEN NO FREQUENCY IS PREDICTED BY EQUATION 8

---

By taking the factor of  $U/D$  to the left-hand side

$$\frac{fD}{U} = \sqrt{\left(c^* - \frac{a_1}{2m^*}\right)^2 - 4\left(\frac{2\pi}{U^*}\right)^2}. \quad (4.4)$$

Expanding terms gives

$$\frac{fD}{U} = \sqrt{c^{*2} - \frac{2c^*a_1}{2m^*} + \frac{a_1^2}{4m^{*2}} - \frac{16\pi^2}{U^{*2}}}. \quad (4.5)$$

Multiplying through by  $m^{*2}$  gives

$$\frac{fD}{U} = \sqrt{c^{*2}m^{*2} - c^*m^*a_1 + \frac{a_1^2}{4} - \frac{16\pi^2m^{*2}}{U^{*2}}}. \quad (4.6)$$

By substituting  $\Pi_1$  and  $\Pi_2$  appropriately the expression of the linear frequency reduced to

$$\frac{fD}{U} = \sqrt{\Pi_2^2 - \Pi_2a_1 + \frac{a_1^2}{4} - 4\Pi_1}. \quad (4.7)$$

Thus, from equation 4.7 the non-dimensionalised linear frequency of the system could be expressed from the newly formulated terms,  $\Pi_1$  and  $\Pi_2$ .

So, by setting  $f = 0$ , the relationship between  $\Pi_1$  and  $\Pi_2$  at the limit can be found.

### 4.3 Finding the terminal velocity of the body when no frequency is predicted by equation 8

For very small  $Pi_1$  where no frequency is predicted by equation 8, we can assume that the body quickly accelerates to a velocity where the lift force is balanced by the damping force. While the displacement is small, the spring force is basically negligible. Also, for the velocity to saturate (reach a constant value), we need only one nonlinear term in the equation, and so we retain only up to the cubic velocity term in the lift force to give

$$c\dot{y} = \frac{1}{2}\rho U^2 \mathcal{A} \left[ a_1 \left( \frac{\dot{y}}{U} \right) + a_3 \left( \frac{\dot{y}}{U} \right)^3 \right]. \quad (4.8)$$

Rearranging and dividing by  $\dot{y}$  gives

$$\left( \frac{1}{2}\rho U \mathcal{A} a_1 - c \right) + \frac{1}{2}\rho \frac{1}{U} \mathcal{A} a_3 \dot{y}^2 = 0, \quad (4.9)$$

So that the terminal velocity  $\dot{y}$  is given by

$$\dot{y} = \pm \sqrt{-\frac{(1/2)\rho U^2 \mathcal{A} a_1 - cU}{(1/2)\rho \mathcal{A} a_3}}. \quad (4.10)$$

#### 4. FREQUENCY RESPONSE OF THE SYSTEM

---

This can be written as

$$\dot{y} = \pm \sqrt{U^2 \frac{a_1}{a_3} - U^2 \frac{c}{(1/2)\rho U \mathcal{A} a_3}} \quad (4.11)$$

or

$$\frac{\dot{y}}{U} = \pm \sqrt{\frac{a_1}{a_3} - \frac{c}{(1/2)\rho U \mathcal{A} a_3}}. \quad (4.12)$$

Finally, the definition of  $\Pi_2$  can be substituted into the last term to give

$$\frac{\dot{y}}{U} = \pm \sqrt{\frac{1}{a_3}(a_1 - 2\Pi_2)}, \quad (4.13)$$

hence the terminal, or maximum velocity is a function of  $\Pi_2$  only.

## CHAPTER 5

---

# INFLUENCE OF FLUID DYNAMICS OF THE SYSTEM ON THE EXTRACTED POWER

### 5.1 Introduction

This chapter contains the results and discussion relating to the third objective of this thesis. As discussed in chapter 1 the induced force  $F_y$  of the system is a result of the top and bottom of the shear layer behaviour of the system. The current published work shows that the afterbody of the system has a significant influence on the galloping response. In this chapter, the influence of shear layer behaviour and hence, the influence of the afterbody on mean extracted power is discussed.

Here, the influence of shear layer on the mean power is studied by introducing a cross section which is a hybrid of a square and a triangle. Data are analysed the cross section is transformed gradually by manipulating the ratio of two length scales.

The stationary forcing data is presented for each cross section followed by the QSS power curves. Based on the QSS power data, an optimum cross section for power extraction is identified. Next, the underpinning reason for the negative portion of certain  $C_y$  curves is discussed through surface pressure and flow velocity data. Following this, a reasoning for the discrepancy between QSS and DNS mean power at the optimum power cross section is

discussed.

A final summary is presented explaining the influence of the shear layer on mean power output and the preliminary design considerations to optimise the fluid mechanics to obtain an optimum power output.

### 5.2 Influence of the shear layers

As highlighted in section 1.2.5 the afterbody of the cross section has a significant influence on galloping. This is because of the shear layer need to interact with the afterbody after separation at the leading edge.

The  $C_y$  vs  $\alpha$  curve increases reaches a maximum and reduces as the induce angle is increased. The maximum of the induced lift occurs when the separated shear layer (at the leading edge) closer to the surface of the body reattaches at the trailing edge. Therefore, by delaying the reattachment the point where the maximum lift occurs can be shifted towards a higher induced angle which leads to a higher induced velocity. As shown in equation 2.2 higher velocity leads to higher power output. In order to test this hypothesis the shear layer reattachment was reduced by gradually tapering off the top and bottom sides of the square cross section as sown in figure 5.1. The  $\frac{d}{l}$  was changed gradually from 1 to zero at increments of 0.25 where 1 being the square cross section and 0 being an isosceles triangle.

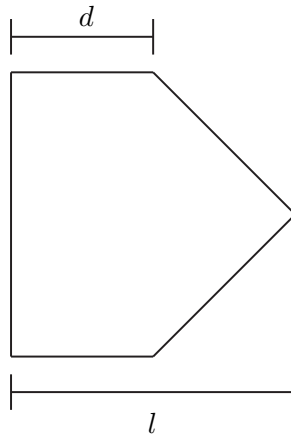


Figure 5.1: Illustration of the hybrid cross section (combination of a square and a triangle) obtained by tapering the afterbody of the square. The afterbody was changed by changing the ratio of  $\frac{d}{l}$ . Hence, data were obtained for  $\frac{d}{l} = 1, 0.75, 0.5, 0.25$  and 0.



### 5.3 Static body results

$\frac{d}{l}$	$a_1$	$a_3$	$a_5$	$a_7$	
0	-2.30617	-269.075	-59.2929	4.74389	20.5° – 23.5°
	-5.08342	-56.5390	-160.505	-105.773	28.6° – 28.7°
	4.40685	19.9213	22.8894	7.68556	
0.25	-0.605146	-19.4346	-82.4463	-94.4226	30.1° – 30.2°
	2.50538	9.91021	10.2712	3.94112	
0.5	1.44734	4.83885	-166.900e	-983.072	14° – 16°
	1.51455e	15.8476	52.5465	62.8067	
0.75	1.76938	35.2630	-345.562	-10072.7	11.03° – 11.11°
	1.77553	43.0120	262.983	638.484	

Table 5.1: Coefficient values used in the 7th order interpolation polynomial at  $Re = 200$ . Data present for  $\frac{d}{l} = 0 - 0.75$  at increments of 0.5. Multiples polynomials were used to attain a better fit. The plot of the compound fit is presented in figure 5.2.

Stationary  $C_y$  results were obtained for cross sections where  $\frac{d}{l} = 1, 0.75, 0.5, 0.25, 0$ . Where  $\frac{d}{l} = 1$  being the square and  $\frac{d}{l} = 0$  being an isosceles triangle. Table 5.1 shows the coefficients of the 7<sup>th</sup> order interpolation polynomial for each cross section. In order to achieve a better fit, piecewise interpolation using multiple 7<sup>th</sup> order polynomials were incorporated for a single cross section. During the curve fitting process more importance

## 5. INFLUENCE OF FLUID DYNAMICS OF THE SYSTEM ON THE EXTRACTED POWER

---

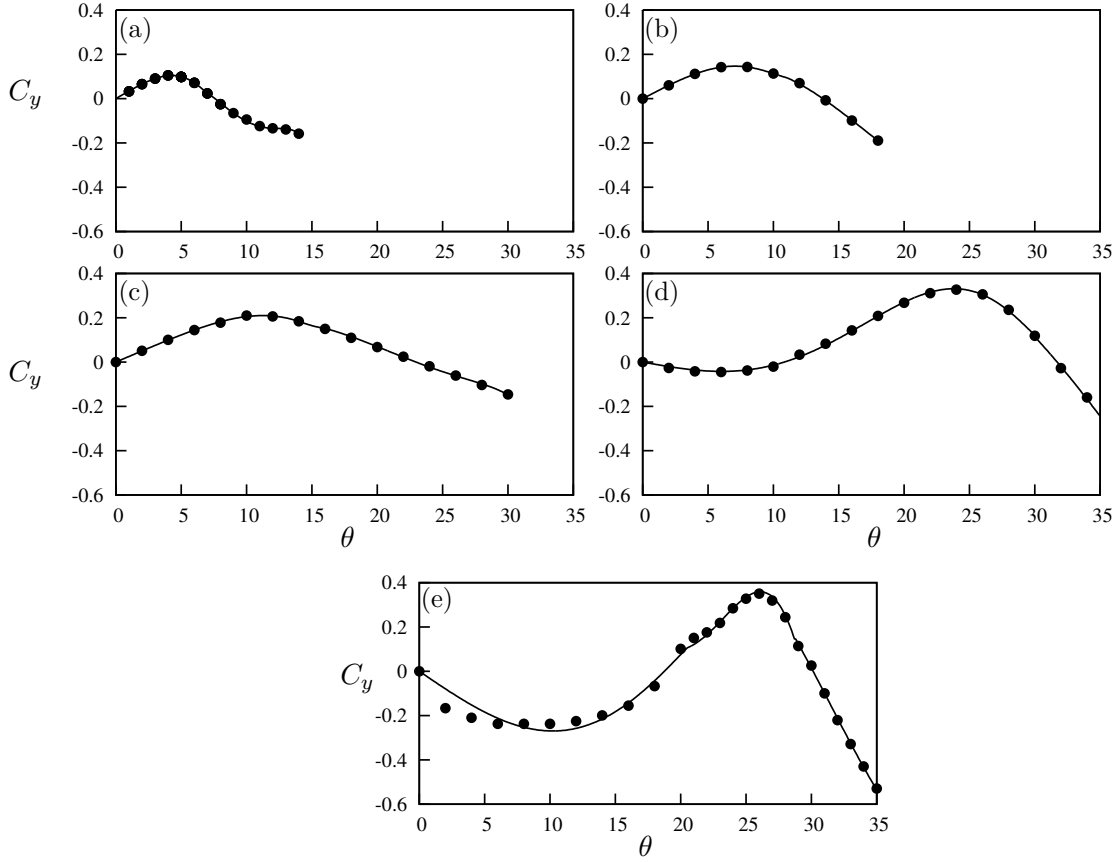


Figure 5.2: Induced lift coefficient  $C_y$  at different angles for selected cross sections. Data presented for cross sections, (a) square, (b)  $\frac{d}{l} = 0.75$ , (c)  $\frac{d}{l} = 0.5$ , (d)  $\frac{d}{l} = 0.25$  and (e) triangle. Points ( $\bullet$ ) are measurements from the static body simulations and the curves are the compound 7<sup>th</sup> order polynomials.

was given to the positive portion of the  $C_y$  curve as this portion of the data ensures that the galloping is sustained.

The  $C_y$  vs.  $\alpha$  curves in figure 5.2 shows that the peak value of  $C_y$  shifts to the right as  $\theta$  is increased. As  $\theta$  is proportional to the transverse velocity of the body  $\tan\theta = \frac{\dot{y}}{U}$ , it is clear that the maximum  $C_y$  occur at higher velocities as  $\frac{d}{l}$  is decreased which was an expected outcome. Another interesting observation is that the presence of a negative portion prior to the point of maximum  $C_y$  in the  $C_y$  vs.  $\theta$  curves as  $\frac{d}{l}$  is decreased. In this region,  $C_y$  decreases reaches a minimum and then increases as  $\theta$  is increased. The absolute value of the maximum is greater than the absolute value of the minimum. This negative portion starts to emerge at  $\frac{d}{l} = 0.25$ . However, the maximum value of  $C_y$  increases as  $\frac{d}{l}$

is decreased providing an indication of a possibility of attaining a higher power output at low  $\frac{d}{l}$ .

Yet, it is to be noted that the presence of the negative portion of the lift curve will oppose the motion of the body where the velocity of the body and the driving force will be out of phase. This will lead to an energy transfer from the body to the fluid which is the opposite of the expectations resulting a reduction in mean power output.

## 5.4 QSS results

### 5.4.1 Mean power output

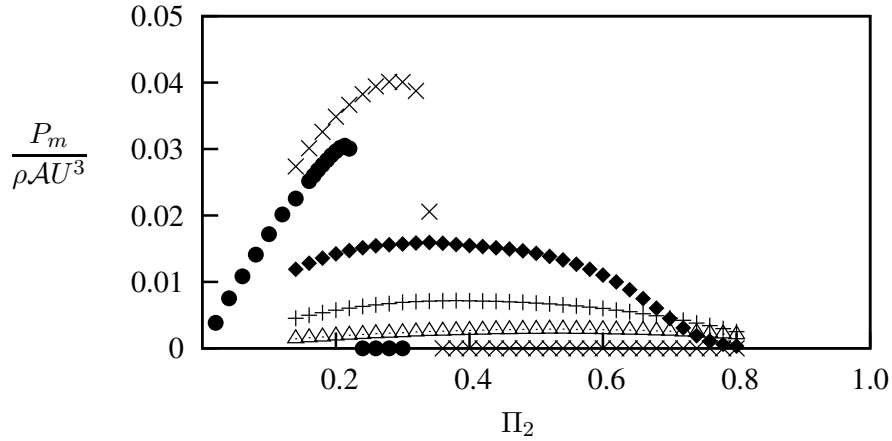


Figure 5.3: Dimensionless mean power obtained using QSS model as a function of  $\Pi_2$ . Data presented for five selected cross sections, square ( $\triangle$ ),  $\frac{d}{l} = 0.75$  ( $+$ ),  $\frac{d}{l} = 0.5$  ( $\blacklozenge$ ),  $\frac{d}{l} = 0.25$  ( $\times$ ) and triangle ( $\bullet$ ) at  $Re = 200$ ,  $\Pi_1 = 100$ .

Figure 5.3 shows the mean power  $\Pi_2$  vs. mean power for different cross sections namely  $\frac{d}{l} = 1, 0.75, 0.5, 0.25$  and  $0$ . The shear layer reattachment is decreased as  $\frac{d}{l}$  is decreased. The mean power increases as  $\frac{d}{l}$  is decrease where a significant increase in the maximum power could be observed. This meets the expectations where it was hypothesised that the mean power would increase as the shear layer re-attachment is delayed. A rapid increase in mean power could be observed below  $\frac{d}{l} = 0.5$ .

As  $\frac{d}{l}$  decreases beyond  $0.25$ , as the mean power reaches the maximum a sudden drop could be observed as  $\Pi_2$  is increased (eg.  $\Pi_2 = 0.39$  for  $\frac{d}{l} = 0.25$ ). One interesting fact

## 5. INFLUENCE OF FLUID DYNAMICS OF THE SYSTEM ON THE EXTRACTED POWER

---

which could be observed is that the maximum power at  $\frac{d}{l} = 0.25$  is larger than  $\frac{d}{l} = 0$ . This is against the expected outcome as the hypothesis was that by delaying the shear layer reattachment a higher mean power output could be gained.

It is clear that as discussed in section 5.3 the negative portion of the  $C_y$  curve influences this reduction in maximum power at  $\frac{d}{l} = 0$  in comparison with  $\frac{d}{l} = 0.25$ . Comparing the initial negative portion of the  $C_y$  vs  $\theta$  plot of  $\frac{d}{l} = 0.25$  and  $\frac{d}{l} = 0$  cross section, it is clear that the area of the initial negative region is high in  $\frac{d}{l} = 0$  which effectively transfers large amount of energy from the body to the fluid and therefore resulting a low power output.

### 5.4.2 Surface pressure

In order to investigate further the cause of this negative region, surface pressure data of static DNS simulations were analysed of the isosceles triangle ( $\frac{d}{l} = 0$ ) at  $\theta = 4^\circ$ ,  $\theta = 16^\circ$  and  $\theta = 21^\circ$ . These points lie in regions where the negative portion increases, the negative portion decreases and where  $C_y$  becomes positive respectively.

Figure 5.4 shows the surface pressure of the top and bottom surfaces of the body ( $\frac{d}{l} = 0$ ) starting from the leading edges. At  $\theta = 4^\circ$  The pressure of the bottom of the body is greater than the top. Therefore, a pressure difference is created and a force is generated in the upward direction which according to the sign convention presented in 1.1, against the velocity of the body, hence giving a negative  $C_y$ . As  $\theta$  (figure 5.4 (b)) is increased, at  $16^\circ$  the gap between the surface pressure at the leading edge between the top and the bottom reduces. This effect results the increase in  $C_y$  (although it is still in the negative region). As  $\theta$  is further increased at  $21^\circ$  (figure 5.4 (c)) the surface pressure on the top side becomes greater than the bottom. Therefore, the net effect of the pressure difference is a positive  $C_y$  which the driving force  $F_y$  is in phase with the velocity of the body.

### 5.4.3 Velocity profiles at the leading edges

Having established that the cause of the initial negative region of the  $C_y$  vs.  $\theta$  plot was the pressure difference mainly at the leading edge of the top and bottom surfaces of the cross section, it was then further investigated the cause of this particular pressure difference.

A key variable which directly relates to the pressure fluid in motion is the velocity of the fluid. The fundamentals of fluid dynamics state that pressure and velocity have

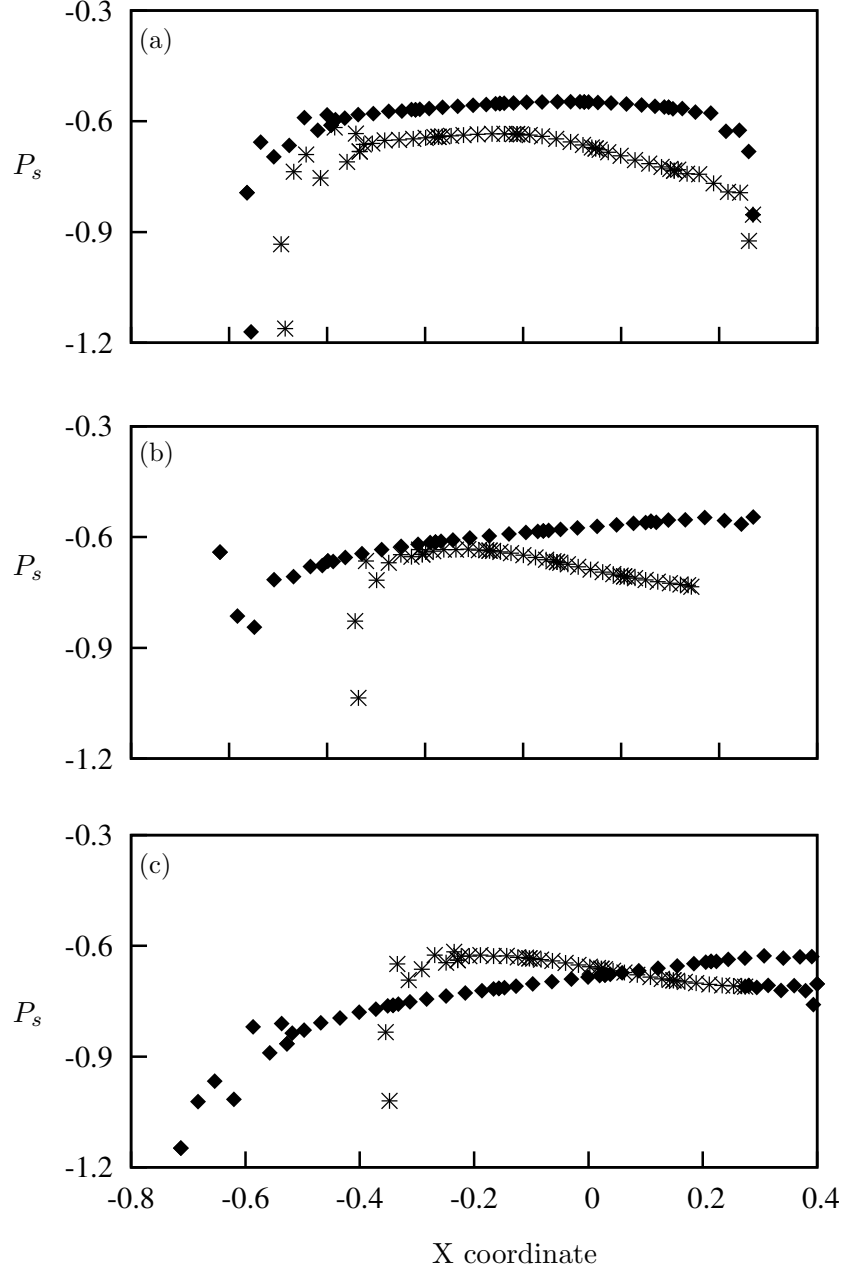


Figure 5.4: Surface pressure of top ( $\times$ ) and bottom ( $\blacklozenge$ ) surfaces of the static triangular cross section at (a)  $\theta = 4^\circ$ , (b)  $\theta = 16^\circ$  and (c)  $\theta = 21^\circ$ . A clear pressure difference is visible between the surfaces. The top surface comparatively has more negative pressure where a lift is created which results in a negative  $C_y$  at  $4^\circ$  and reduces as  $\theta$  is increased, while the vice versa occurs at the top surface.

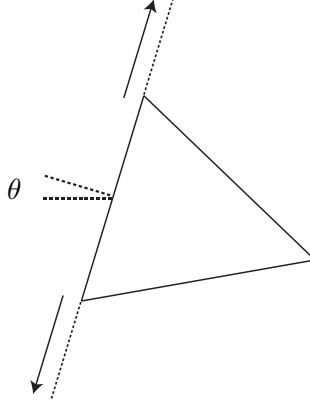


Figure 5.5: Illustration of the lines along which the flow velocity magnitudes have been extracted. The data have been extracted along a line starting from the separation points in the outward direction (shown with arrows) for the top and bottom surfaces.

an inversely proportional relationship in a Newtonian fluid. This is also evident in the Bernoulli's equation. Hence, analysis of the velocity at the edges of flow separation was performed to obtain a clear understanding about the cause of the pressure differences occurred.

In order to obtain a clear picture of the behaviour of the velocity, velocity magnitude data were obtained along lines spreading outwards starting from the top and bottom edges of flow separation. A clear illustration of these lines are depicted in figure 5.5. The lengths of these lines were equal to unity (equal to the frontal projected height of the body). Data were obtained for the same cases which the surface pressure data were obtained i.e. isosceles triangle ( $\frac{d}{l} = 0$ ) at  $\theta = 4^\circ$ ,  $\theta = 16^\circ$  and  $\theta = 21^\circ$ .

The velocity profiles at the chosen three incident angles are presented in 5.6. A sudden rise of velocity magnitude could be observed at the flow separation points. The velocity magnitude at the top separation point at  $\theta = 4^\circ$  (figure 5.6 (a)) is less than the bottom separation point, leading to a lower pressure at the top edge. However, the velocity magnitude at the bottom edge becomes greater than the top edge at  $\theta = 16^\circ$ . The difference between the velocity magnitude tends to broaden as  $\theta$  is increased to  $21^\circ$ , while the velocity magnitude at the bottom being greater than the top (figure 5.6 (c)). This effectively creates the pressure difference created in figure 5.4 (c), which leads to a positive  $C_y$  and results in

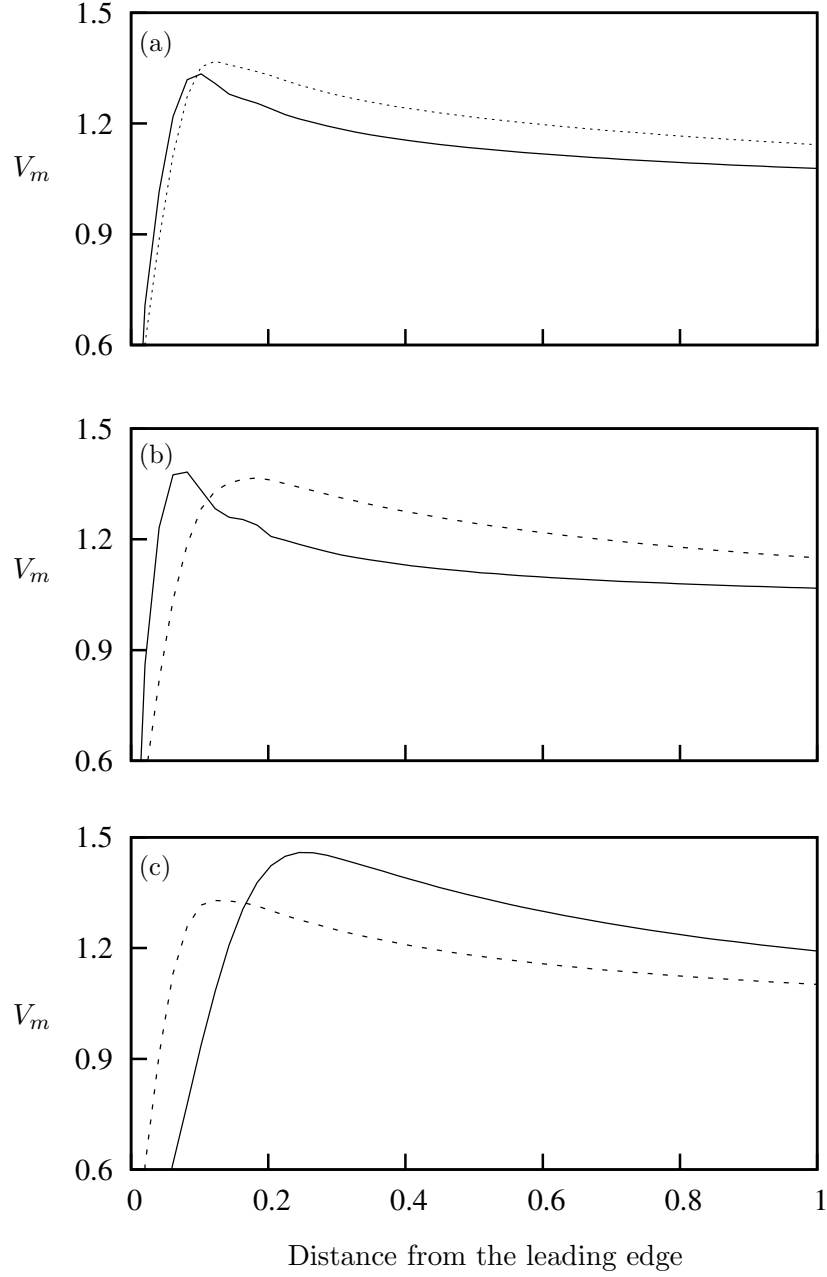


Figure 5.6: Velocity magnitudes of the flow along a line parallel to the front surface spreading towards top (---) and bottom (—) boundaries (figure 5.5). These two lines (for the top and bottom surfaces) start from the top and bottom leading edges of the triangular cross section. Data present (a)  $\alpha = 4^\circ$ , (b)  $\alpha = 16^\circ$  and (c)  $\alpha = 21^\circ$ .

a forcing which is in phase with the velocity of the body.

## 5.5 Fluid-structure interaction (DNS) results

As discussed in section 3.3.5 the main drawback of the QSS model is assuming that the only driving force of the system is  $F_y$ , which is generated from induced velocity. However, it was proved that this is not the case as vortex shedding have a significant influence with other non-linear disturbances on mean power as  $\Pi_1$  decreases. Nevertheless, it was also concluded that a good agreement for power could be made at high  $\Pi_1$  for the square cross section. Therefore, a comparison study between QSS and DNS mean power was carried out on the different cross section at high  $\Pi_1$  ( $= 1000$ ). As it was evident from figure 5.3 that the maximum power at  $\frac{d}{l} = 0 < \frac{d}{l} = 0.25$  DNS mean power was between  $0.25 \leq \frac{d}{l} \leq 1$ .

Both DNS and QSS mean power data figure 5.7 show that  $\frac{d}{l}$  decreases maximum mean extracted power increases following a similar trend. Thus these results reinforce the hypothesis for this section which is obtaining higher mean power by delaying the flow re-attachment.

However, a significant error calculated using equation 3.9 between QSS and DNS power could be observed as  $\frac{d}{l}$  increased. The quantified errors presented in 5.8 clearly shows the exponential increase in the % error as  $\frac{d}{l} \rightarrow 0.25$



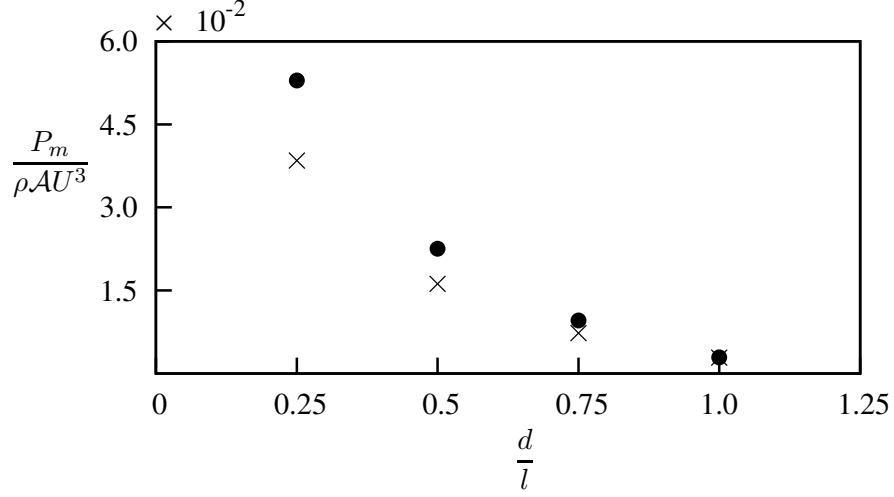


Figure 5.7: Comparison of the maximum power obtained using DNS ( $\bullet$ ) data and predicted by QSS ( $\times$ ) model as a function of  $\frac{d}{l}$ . Data obtained at  $\Pi_1 = 1000$  ( $m^* = 201.3$ ) and  $Re = 200$ . Similar trends are present for both QSS and DNS data. A significant reduction in power could be observed as  $\frac{d}{l} \rightarrow 1$

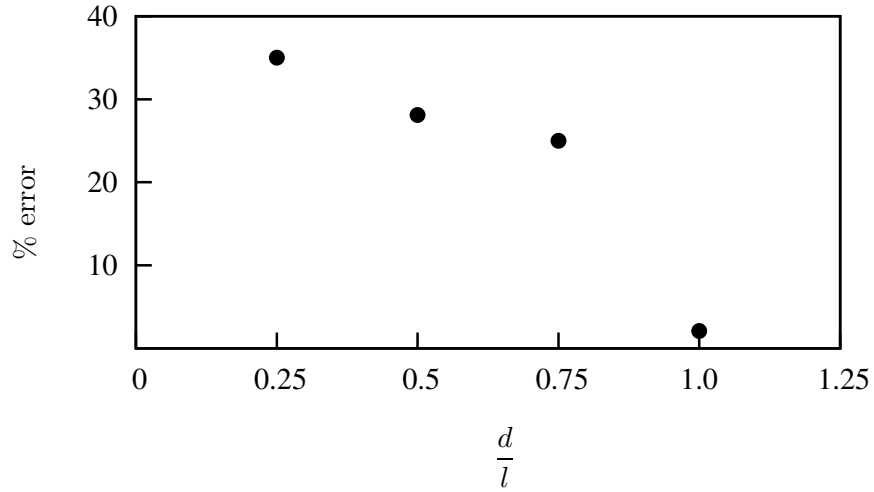


Figure 5.8: The percentage error between the maximum power obtained using DNS data and predicted by QSS model as a function of  $\frac{d}{l}$ . The error reduces significantly as  $\frac{d}{l} \rightarrow 1$

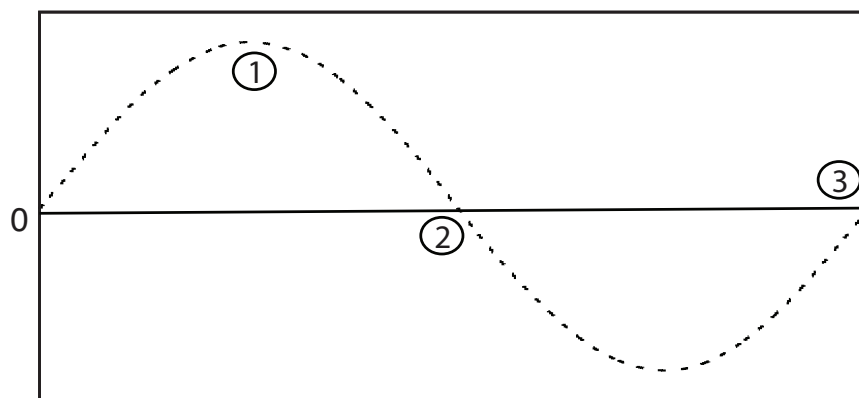


Figure 5.9:

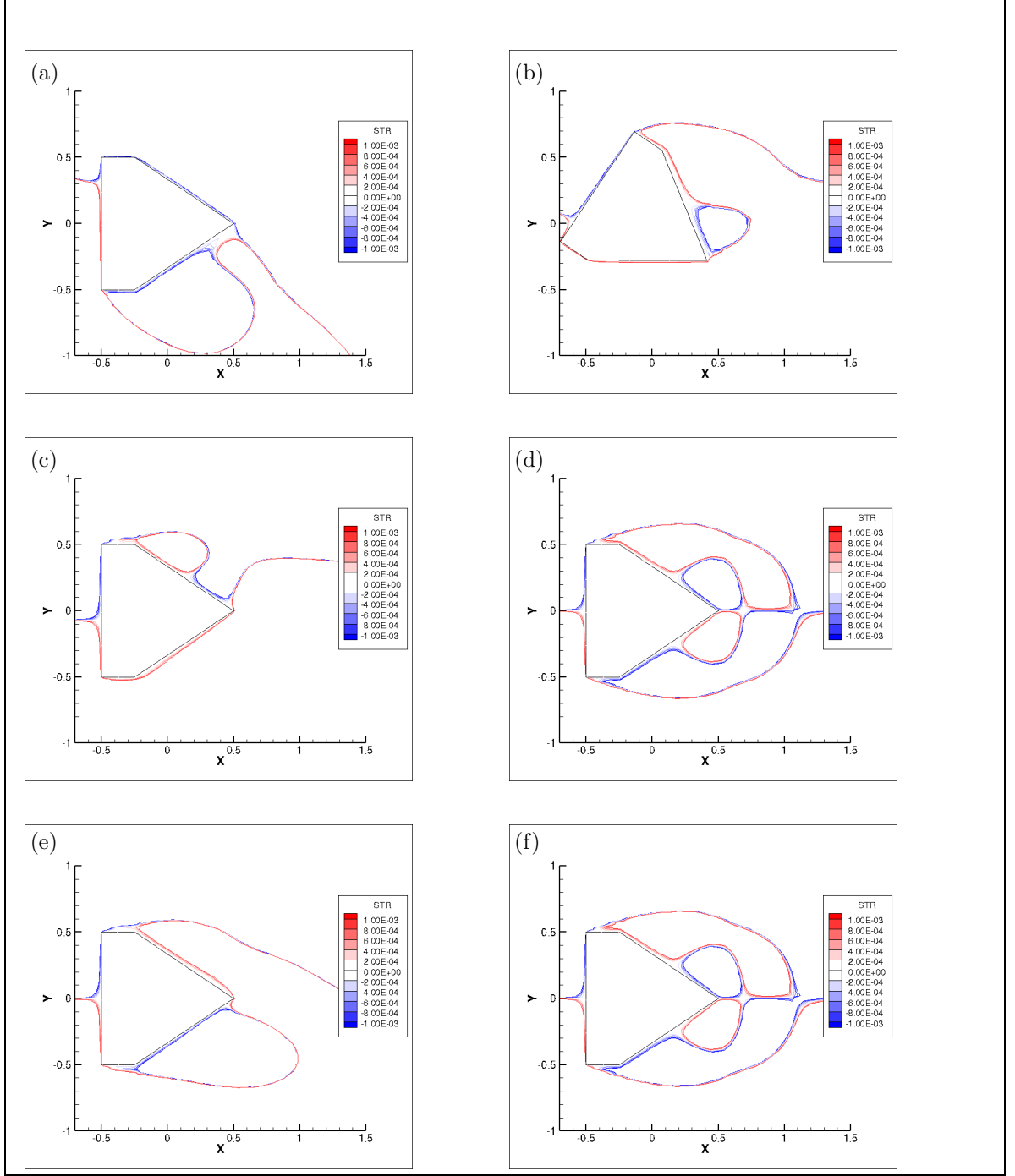


Figure 5.10: Time averaged stream functions of stationary and oscillating flow-fields of the hybrid cross section ( $\frac{d}{l} = 0.25$ ), averaged over a vortex shedding cycle. (a), (c) and (e) the averaged stream functions of the oscillating case at  $t = 2295.763$ ,  $t = 2305.897$  and  $t = 2325.870$ . (b), (d) and (f) are the stream functions of the flow field of the stationary body corresponding to the induced angles of (a), (c) and (e).



# BIBLIOGRAPHY

---

- Alonso, G., Meseguer, J., Pérez-Grande, I., 2005. Galloping instabilities of two-dimensional triangular cross-section bodies. *Experiments in Fluids* 38, 789–795.
- Alonso, G., Meseguer, J., Sanz-Andrés, A., Valero, E., 2010. On the galloping instability of two-dimensional bodies having elliptical cross-sections. *Journal of Wind Engineering and Industrial Aerodynamics* 38, 789–795.
- Alonso, G., Valero, E., Meseguer, J., 2009. An analysis on the dependence on cross section geometry of galloping stability of two-dimensional bodies having either biconvex or rhomboidal cross sections. *European Journal of Mechanics B/Fluids* 28, 328–334.
- Barrero-Gil, A., Alonso, G., Sanz-Andres, A., Jul. 2010. Energy harvesting from transverse galloping. *Journal of Sound and Vibration* 329 (14), 2873–2883.
- Barrero-Gil, A., Sanz-Andrés, A., Roura, M., Oct. 2009. Transverse galloping at low Reynolds numbers. *Journal of Fluids and Structures* 25 (7), 1236–1242.
- Bearman, P. W., Gartshore, I. S., Maull, D. J., Parkinson, G. V., 1987. Experiments on flow-induced vibration of a square-section cylinder. *Journal of Fluids and Structures* 1, 19–34.
- Bernitsas, M. M., Ben-Simon, Y., Raghavan, K., Garcia, E. M. H., 2009. The VIVACE Converter: Model Tests at High Damping and Reynolds Number Around  $10^5$ . *Journal of Offshore Mechanics and Arctic Engineering* 131 (1), 011102.
- Bernitsas, M. M., Raghavan, K., Ben-Simon, Y., Garcia, E. M. H., 2008. VIVACE (Vortex Induced Vibration Aquatic Clean Energy): A new concept in generation of clean and

## BIBLIOGRAPHY

---

- renewable energy from fluid flow. *Journal of Offshore Mechanics and Arctic Engineering* 130 (4), 041101–15.
- Blevins, R. D., 1990. *Flow-Induced Vibration*, 2nd Edition. New York: Van Nostrand Reinhold.
- Bouclin, D. N., 1977. Hydroelastic oscillations of square cylinders. Master's thesis, University of British Columbia.
- Den Hartog, J. P., 1956. *Mechanical Vibrations*. Dover Books on Engineering. Dover Publications.
- Deniz, S. and Staubli, T., 1997. Oscillating rectangular and octagonal profiles: Interaction of leading-and trailing-edge vortex formation. *Journal of Fluids and Structures* 11, 3–31.
- Fletcher, C. A. J., 1984. *Computational Galerkin methods*. Springer-Verlag, New York.
- Fletcher, C. A. J., 1991. *Computational techniques for fluid dynamics*. Vol. 1. Springer-Verlag, New York. Gabbai,.
- Glauert, H., 1919. The rotation of an aerofoil about a fixed axis. Tech. rep., Advisory Committee on Aeronautics R and M 595. HMSO, London.
- Gresho, P. M., Sani, R. L., 1987. On pressure boundary conditions for the incompressible Navier–Stokes equations. *International journal for numerical methods in fluids* 7, 1111–1145.
- Griffith, M. D., Leontini, J. S., Thompson, M. C., Hourigan, K., 2011. Vortex shedding and three-dimensional behaviour of flow past a cylinder confined in a channel. *Journal of Fluids and Structures* 27 (5-6), 855–860.
- Joly, A., Etienne, S., Pelletier, D., Jan. 2012. Galloping of square cylinders in cross-flow at low Reynolds numbers. *Journal of Fluids and Structures* 28, 232–243.
- Karniadakis, G. E., Sherwin, S., 2005. *Spectral/hp element methods for computational fluid dynamics*, ii Edition. Oxford University.
- Kreyszig, E., 2010. *Advanced Engineering Mathematics*, 10th Edition. John Wiley & Sons.

- Lee, J., Bernitsas, M., Nov. 2011. High-damping, high-Reynolds VIV tests for energy harnessing using the VIVACE converter. *Ocean Engineering* 38 (16), 1697–1712.
- Lee, J., Xiros, N., Bernitsas, M., Apr. 2011. Virtual damperspring system for VIV experiments and hydrokinetic energy conversion. *Ocean Engineering* 38 (5-6), 732–747.
- Leontini, J. S., Lo Jacono, D., Thompson, M. C., Nov. 2011. A numerical study of an inline oscillating cylinder in a free stream. *Journal of Fluid Mechanics* 688, 551–568.
- Leontini, J. S., Thompson, M. C., 2013. Vortex-induced vibrations of a diamond cross-section: Sensitivity to corner sharpness. *Journal of Fluids and Structures* 39, 371–390.
- Leontini, J. S., Thompson, M. C., Hourigan, K., Apr. 2007. Three-dimensional transition in the wake of a transversely oscillating cylinder. *Journal of Fluid Mechanics* 577, 79.
- Luo, S., Chew, Y., Ng, Y., Aug. 2003. Hysteresis phenomenon in the galloping oscillation of a square cylinder. *Journal of Fluids and Structures* 18 (1), 103–118.
- Nakamura, Y., Mizota, T., 1975. Unsteady lifts and wakes of oscillating rectangular prisms. *ASCE Journal of the Engineering Mechanics Division* 101, 855–871.
- Nakamura, Y., Tomonari, Y., 1977. Galloping of rectangular prisms in a smooth and in a turbulent flow. *Journal of Sound and Vibration* 52, 233–241.
- Naudascher, E., Wang, Y., 1993. Flow induced vibrations of prismatic bodies and grids of prisms. *Journal of fluids and structures* 7, 341–373.
- Ng, Y., Luo, S., Chew, Y., Jan. 2005. On using high-order polynomial curve fits in the quasi-steady theory for square-cylinder galloping. *Journal of Fluids and Structures* 20 (1), 141–146.
- Païdoussis, M., Price, S., de Langre, E., 2010. *Fluid-Structure Interactions : Cross-Flow-Induced Instabilities*. Cambridge University Press.
- Parkinson, G., 1989. Phenomena and modelling of flow-induced vibrations of bluff bodies. *Progress in Aerospace Sciences* 26, 169–224.
- Parkinson, G., Brooks, N. P. H., 1961. On the aeroelastic instability of bluff cylinders. *Journal of Applied Mechanics* 28, 252–258.

## BIBLIOGRAPHY

---

- Parkinson, G. V., 1974. Mathematical models of flow-induced vibrations of bluff bodies. In *Flow-Induced Structural Vibrations*, e. naudascher Edition. Berlin: SpringerVerlag.
- Parkinson, G. V., Smith, J. D., 1964. The square prism as an aeroelastic non-linear oscillator. *The Quarterly Journal of Mechanics and Applied Mathematics* 17 (2), 225–239.
- Pregalato, C., 2003. Flow-induced vibrations of a tethered sphere. Ph.D. thesis, Monash University.
- Raghavan, K., Bernitsas, M., Apr. 2011. Experimental investigation of Reynolds number effect on vortex induced vibration of rigid circular cylinder on elastic supports. *Ocean Engineering* 38 (5-6), 719–731.
- Raghavan, K., Bernitsas, M. M., Maroulis, D. E., 2009. Effect of Bottom Boundary on VIV for Energy Harnessing at  $8 \times 10^3 < Re < 1.5 \times 10^5$ . *Journal of Offshore Mechanics and Arctic Engineering* 131 (3), 031102.
- Robertson, I., Li, L., Sherwin, S. J., Bearman, P. W., 2003. A numerical study of rotational and transverse galloping rectangular bodies. *Journal of Fluids and Structures* 17, 681 – 699.
- Ruscheweyh, H., Hortmanns, M., Schnakenberg, C., 1996. Vortex-excited vibrations and galloping of slender elements. *Journal of Wind Engineering and Industrial Aerodynamics* 65, 347–352.
- Sheard, G. J., Fitzgerald, M. J., Ryan, K., Jun. 2009. Cylinders with square cross-section: wake instabilities with incidence angle variation. *Journal of Fluid Mechanics* 630, 43.
- Thompson, M., Hourigan, K., Sheridan, J., Feb. 1996. Three-dimensional instabilities in the wake of a circular cylinder. *Experimental Thermal and Fluid Science* 12 (2), 190–196.
- Thompson, M. C., Hourigan, K., Cheung, A., Leweke, T., Nov. 2006. Hydrodynamics of a particle impact on a wall. *Applied Mathematical Modelling* 30 (11), 1356–1369.
- Tong, X., Luo, S., Khoo, B., Oct. 2008. Transition phenomena in the wake of an inclined square cylinder. *Journal of Fluids and Structures* 24 (7), 994–1005.



- Tu, J., Yeoh, G., Liu, C., 2008. Computational Fluid Dynamics: A Practical Approach, 1st Edition. Butterworth-Heinemann.
- Vicente-Ludlam, D., Barrero-Gil, A., Velazquez, A., 2014. Optimal electromagnetic energy extraction from transverse galloping. *Journal of Fluids and Structures* 51, 281–291.
- Vio, G., Dimitriadis, G., Cooper, J., Oct. 2007. Bifurcation analysis and limit cycle oscillation amplitude prediction methods applied to the aeroelastic galloping problem. *Journal of Fluids and Structures* 23 (7), 983–1011.
- Weaver, D. S., Veljkovic, I., 2005. Vortex shedding and galloping of open semi-circular and parabolic cylinders in cross-flow. *Journal of Fluids and Structures* 21, 65–74.
- White, F., 1999. Fluid mechanics, 4th Edition. McGraw-Hill, Boston.